VEHICLE SYSTEM DYNAMICS, 2016
VOL. 54, NO. 8, 1147–1176
http://dx.doi.org/10.1080/00423114.2016.1193209

IAVSD
Taylor & Francis
Taylor & Francis Group

Connected cruise control: modelling, delay effects, and nonlinear behaviour

Gábor Orosz

Department of Mechanical Engineering, University of Michigan, Ann Arbor, MI, USA

ABSTRACT

Connected vehicle systems (CVS) are considered in this paper where vehicles exchange information using wireless vehicle-to-vehicle (V2V) communication. The concept of connected cruise control (CCC) is established that allows control design at the level of individual vehicles while exploiting V2V connectivity. Due to its high level of modularity the proposed design can be applied to large heterogeneous traffic systems. The dynamics of a simple CVS is analysed in detail while taking into account nonlinearities in the vehicle dynamics as well as in the controller. Time delays that arise due to intermittencies and packet drops in the communication channels are also incorporated. The results are summarised using stability charts which allow one to select control gains to maintain stability and ensure disturbance attenuation when the delay is below a critical value.

ARTICLE HISTORY
Received 20 August 2014
Revised 14 May 2016
Accepted 16 May 2016

KEYWORDS
Connected vehicles; communication delays; string stability; nonlinear dynamics

1. Introduction

Traffic congestion has been increasing monotonously in the last couple of decades and it costs more than $120 billion annually in the United States only.[1] Connected vehicle technologies allow vehicles to obtain traffic information beyond the line of sight and they can provide new ways to manage transportation systems and mitigate congestion. In this paper the potentials and limitations of wireless vehicle-to-vehicles (V2V) communication are investigated in order to maintain smooth flow in transportation systems. These technologies are originally developed for safety applications [2,3] but recent efforts demonstrated their applicability to improve mobility [4–6] and fuel economy.[7]

One way to exploit V2V communication for mobility is creating vehicular platoons where a designated leader is followed by a group of vehicles. In traditional platoon design it is assumed that each vehicle is equipped with radar or other range sensors to monitor the motion of the vehicle immediately ahead and they use wireless communication to monitor the motion of the platoon leader as shown at the top of Figure 1. This strategy is referred as cooperative adaptive cruise control (CACC).[8–17] However, looking at the extremely low penetration rate of CACC, one may argue that such tightly controlled platoons are not feasible in dynamic traffic scenarios. First of all, auto manufacturers are selling individual automobiles and not platoons of vehicles. This demand modular design that allow

CONTACT Gábor Orosz orosz@umich.edu

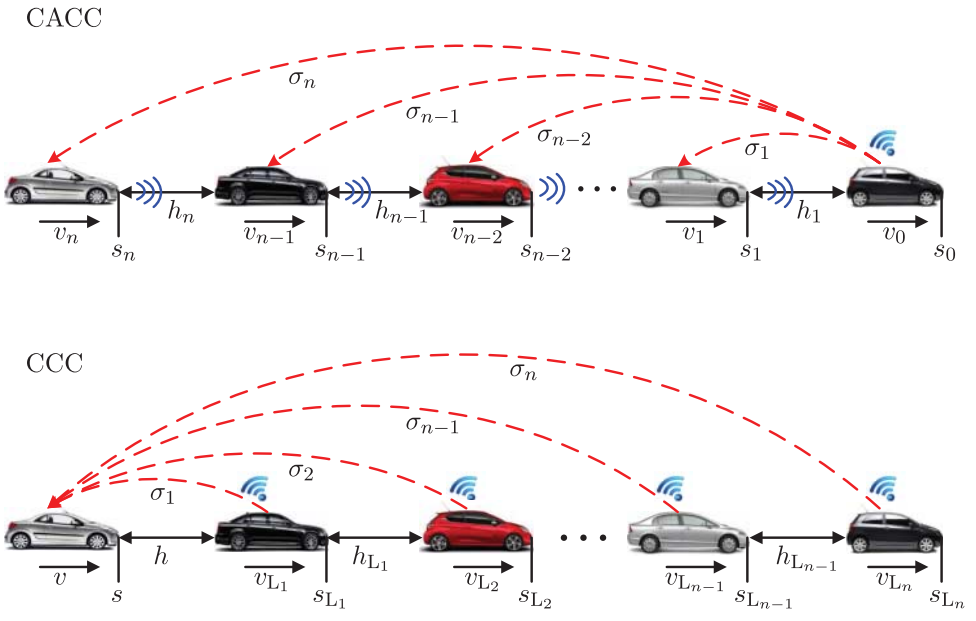

Figure 1. Comparing the connectivity topologies of CACC and CCC where red dashed arrows represent the information flow via wireless V2V communication. In case of CACC each vehicle is equipped by radar and receive information from a designated platoon leader using V2V communication. In case of CCC the vehicle at the tail monitors the motion of *n* vehicles ahead using V2V communication which may be conventional human-driven vehicles. The positions, velocities, and headways of the vehicles are denoted by *s*–s, *v*–s, and *h*–s, respectively, while the communication delays are denoted by σ–s.

auto makers to exploit the received V2V information without designing the whole platoon. Also, the design must remain scalable when increasing the number of vehicles. However, due to the limited range of wireless communication (approxmately 200–300 m), vehicles may not be able to communicate with a distant leader, and long platoons may place strong restrictions on the motion of other vehicles participating in traffic by hindering certain manoeuvres (e.g. entering or leaving the highway). Finally, assuming that all vehicles can be equipped with sensors and actuators is unrealistic and would keep the penetration rate low for a long time. It is clearly necessary to allow human-driven vehicles in the flow that may or may not broadcast information about their motion.

In order to address these challenges we propose the concept of connected cruise control (CCC) that is illustrated at the bottom of Figure 1. This strategy allows a single vehicle benefit from V2V information broadcast by multiple vehicles ahead without requiring those vehicles to be equipped with range sensors. As a matter of fact, it does not even require that all vehicles broadcast their information. The different vehicle numbering used at the top and the bottom of Figure 1 further emphasises that while CACC focuses on building platoons from head to tail, CCC focuses on increasing the situation awareness of an individual vehicle (without redesigning the other vehicles). When comparing the top and bottom of Figure 1 one may also notice that the level of automation required for CCC is much less than for CACC and indeed eliminating range sensors and actuators significantly reduces the cost. Still, our design may bring benefits at the system level when the CCC

vehicle attenuates the velocity fluctuations arising in the vehicles ahead. Moreover, inserting multiple CCC vehicles into the traffic flow of human-driven vehicles does not reduce modularity while the arising large-scale connected vehicle system (CVS) may outperform the conventional system.

Appropriately reacting to events that occur a few vehicles ahead may allowmilder actions that are beneficial for safety and fuel economy and can also improve mobility. To realise CCC, in this paper we propose a class of nonlinear, multi-input, proportional-integral-velocity-acceleration (PIVA) type of controllers that allow the CCC vehicle to exploit all available motion information from the broadcasting vehicles ahead. The controllers are constructed such that they can ensure the existence of a uniform flow equilibrium in the entire velocity range independent of the external disturbances, communication topology, control gains, and communication delays. This makes CCC applicable in heterogenous vehicle streams where CCC vehicles are mixed into the flow of conventional vehicles. Indeed, this increased flexibility makes the control design more challenging as explained below.

Most longitudinal controllers are constructed by omitting vehicle dynamics (grade, air drag, and rolling resistance), but recent efforts showed that this can significantly influence the behaviour of multi-vehicle systems.[18–21]. Here we consider a physics-based nonlinear model to describe the longitudinal vehicle dynamics.[22] Some efforts have been made to eliminate the vehicle dynamics by using controllers that counterbalance these terms.[23] However, since the vehicle parameters may not be known exactly and external disturbances (grade and headwind) may not be known at all, such controllers may not be feasible in practice. Instead, we use integral actions to eliminate the steady-state error. Moreover, controllers are typically designed at the linear level in the CACC literature,[10,14–17] but they ought to contain nonlinearities corresponding the saturation of speed at zero and at the speed limit. In this paper we present a CCC framework that can accommodate any nonlinear range policy. This allows the controllers to switch automatically between CCC and standard cruise control and, by choosing appropriate range policies, can lead to smooth ride conditions and increased highway capacity.

While wireless communication allows vehicles to obtain information beyond the line of sight, it also introduces delays into the control loop due to the intermittencies and packets drops. Current designated short range communication (DSRC) protocols broadcast messages in every 100 ms and the packet delivery ratio varies depending on distance and geography.[24] The arising delays may significantly change the traffic dynamics leading to instabilities at the linear and nonlinear levels.[25–28] In this paper we focus on the two kinds of stability: plant stability and string stability. By plant stability we simply mean the vehicle's ability to approach a constant speed when all vehicles ahead travel with that constant speed. On the other hand, string stability refers the vehicle's ability to attenuate fluctuations arising in the motion of cars ahead. While (plant) stability charts are used extensively in the dynamics and control literature and in the industry, here we also summarise string stability results using stability charts in order to provide a concise representation of the dynamics under parameter variations. Moreover, we also evaluate string stability at the nonlinear level and study how fluctuations of different sizes propagate along the chain of CCC vehicles.

The layout of the paper is the following. In Section 2 we describe our general CCC framework. In Section 3 we analyse the linear dynamics of a simple CVS that is built as

a concatenation of the simplest CCC configuration. In Section 4 we study the nonlinear dynamics of this system. Finally, in Section 5 we conclude our results and discuss future research directions.

2. General framework for CCC

In this section we consider a nonlinear model to describe the longitudinal vehicle dynamics and construct a nonlinear controller that can maintain a distance dependent velocity using V2V information received from up to n vehicles ahead; see the bottom of Figure 1. CCC strategies shall be based on the position, velocity, and acceleration of other vehicles and integral terms shall be included in order to eliminate disturbances like air drag and grade. Thus, we propose a class of multi-input PIVA controllers that can be realised even when not all vehicles in the communication range broadcasts their kinematic information and even when certain type of information (e.g. acceleration) is not available. Moreover, we take into account the delay effects caused by intermittencies and packet drops in wireless communication.

2.1. Vehicle dynamics and traffic equilibrium

In order to model the longitudinal dynamics of the vehicle we assume no slip condition on the wheels and neglect the flexibility of the tires and the suspension. Applying the power law we obtain the differential equation for the longitudinal velocity v

$$m_{\text{eff}}\dot{v} = -mg\sin\phi - \gamma\, mg\cos\phi - k(v+v_{\text{w}})^2 + \frac{\eta}{R}T_{\text{en}}, \tag{1}$$

where the dot stands for differentiation with respect to time t, the effective mass $m_{\text{eff}} = m + J/R^2$ contains the mass of the vehicle m, the moment of inertia J of the rotating elements, and the wheel radius R. Furthermore, g is the gravitational constant, ϕ is the inclination angle, γ is the rolling resistance coefficient, k is the air drag constant, v_{w} is the velocity of the headwind, η is the gear ratio, and T_{en} is the engine torque.[18,22] For simplicity, we consider $\phi = 0$, $v_{\text{w}} = 0$ and $J = 0 \Longrightarrow m_{\text{eff}} = m$, while the other parameters are shown in Table A1 in Appendix 1.

Our goal is to design controllers that can maintain a distance dependent velocity in the velocity range $v \in [0,\ v_{\max}]$ and distance range $h \in [0,\ \infty)$, that is, implement a given range policy $v = V(h)$ as a steady state of the system independent of the external disturbances. While a variety of range policies can be considered they shall satisfy the following general properties: (i) V is continuous and monotonously increasing (the more sparse traffic is, the faster the vehicle wants to go); (ii) $V(h) \equiv 0$ for $h \le h_{\text{st}}$ (in dense traffic, the vehicle intends to stop); (iii) $V(h) \equiv v_{\max}$ for $h \ge h_{\text{go}}$ (in sparse traffic, the vehicle tries to maintain maximum (free-flow) speed). This can formally be written as

$$V(h) = \begin{cases} 0 & \text{if } h \le h_{\text{st}}, \\ F(h) & \text{if } h_{\text{st}} < h < h_{\text{go}}, \\ v_{\max} & \text{if } h \ge h_{\text{go}}, \end{cases} \tag{2}$$

where $F(h)$ is a strictly monotonously increasing function such that $F(h_{\text{st}}) = 0$ and $F(h_{\text{go}}) = v_{\max}$. Indeed, vehicles that implement such range policy are capable of handling

stop-and-go situations. The numerical values of the parameters $h_{\rm st}, h_{\rm go}, v_{\max}$ used in this paper are listed in Table A1 in Appendix 1.

Three different range policies are shown in Figure 2(a)–(c). Panel (a) displays the range policy with the linear function

$$F(h) = v_{\max}\frac{h - h_{\rm st}}{h_{\rm go} - h_{\rm st}}, \tag{3}$$

corresponding to keeping the constant time gap $1/F'(h) \equiv (h_{\rm go} - h_{\rm st})/v_{\max}$. To avoid non-smoothness at $h_{\rm st}$ and $h_{\rm go}$ (that can result in a 'jerky' ride) one may use the smooth range policy with function

$$F(h) = \frac{v_{\max}}{2}\left(1 - \cos\left(\pi\frac{h - h_{\rm st}}{h_{\rm go} - h_{\rm st}}\right)\right), \tag{4}$$

that is shown in Figure 2(b), or the infinitely smooth range policy with function

$$F(h) = \frac{v_{\max}}{2}\left(1 + \tanh\left[\tan\left(\pi\frac{h - (h_{\rm st} + h_{\rm go})/2}{h_{\rm go} - h_{\rm st}}\right)\right]\right), \tag{5}$$

which is depicted in Figure 2(c).

Apart from increasing driver comfort, smooth range policies may also increase the overall throughput of the system as shown by the flux-density diagrams in Figure 2(d)–(f). Here the density and the flux are defined by $\rho = 1/(h + \ell)$ and $Q = \rho v = \rho V(1/\rho - \ell)$ where ℓ is the approximate vehicle length. We remark that these definitions are only accurate in equilibrium situations where equidistant vehicles travel with constant velocity. Using the parameters shown in Table A1, we obtain $q_{\max} = 0.75$ [veh/s/lane] $= 2700$ [veh/h/lane], $q_{\max} = 0.7997$ [veh/s/lane] $= 2879$ [veh/h/lane], and $q_{\max} = 0.8315$ [veh/s/lane] $= 2993$ [veh/h/lane] for the panels (d), (e), and (f), respectively. Such increase is considered significant in transportation systems. At the same time, the minimum of the effective time gap $1/F'(h)$ becomes smaller that can make control design more challenging as explained further below.

2.2. Nonlinear control design

We consider the configuration at the bottom of Figure 1 where the CCC vehicle can monitor the motion of multiple vehicles ahead (up to n vehicles) and we propose the following nonlinear multi-input PIVA controller to regulate the engine torque:

$$T_{\rm en}(t) = \sum_{j=1}^{n} T_{{\rm com},j}(t - \sigma_j), \tag{6}$$

where

$$T_{{\rm com},j} = K_{{\rm p}_j}\dot{z}_j + K_{{\rm i}_j}z_j + K_{{\rm v}_j}(W(v_{{\rm L}_j}) - v) + K_{{\rm a}_j}\dot{v}_{{\rm L}_j}, \tag{7}$$

and

$$\dot{z}_j = V\left(\frac{1}{j}\left(s_{{\rm L}_j} - s - \sum_{k=1}^{j}\ell_{{\rm L}_k}\right)\right) - v, \tag{8}$$

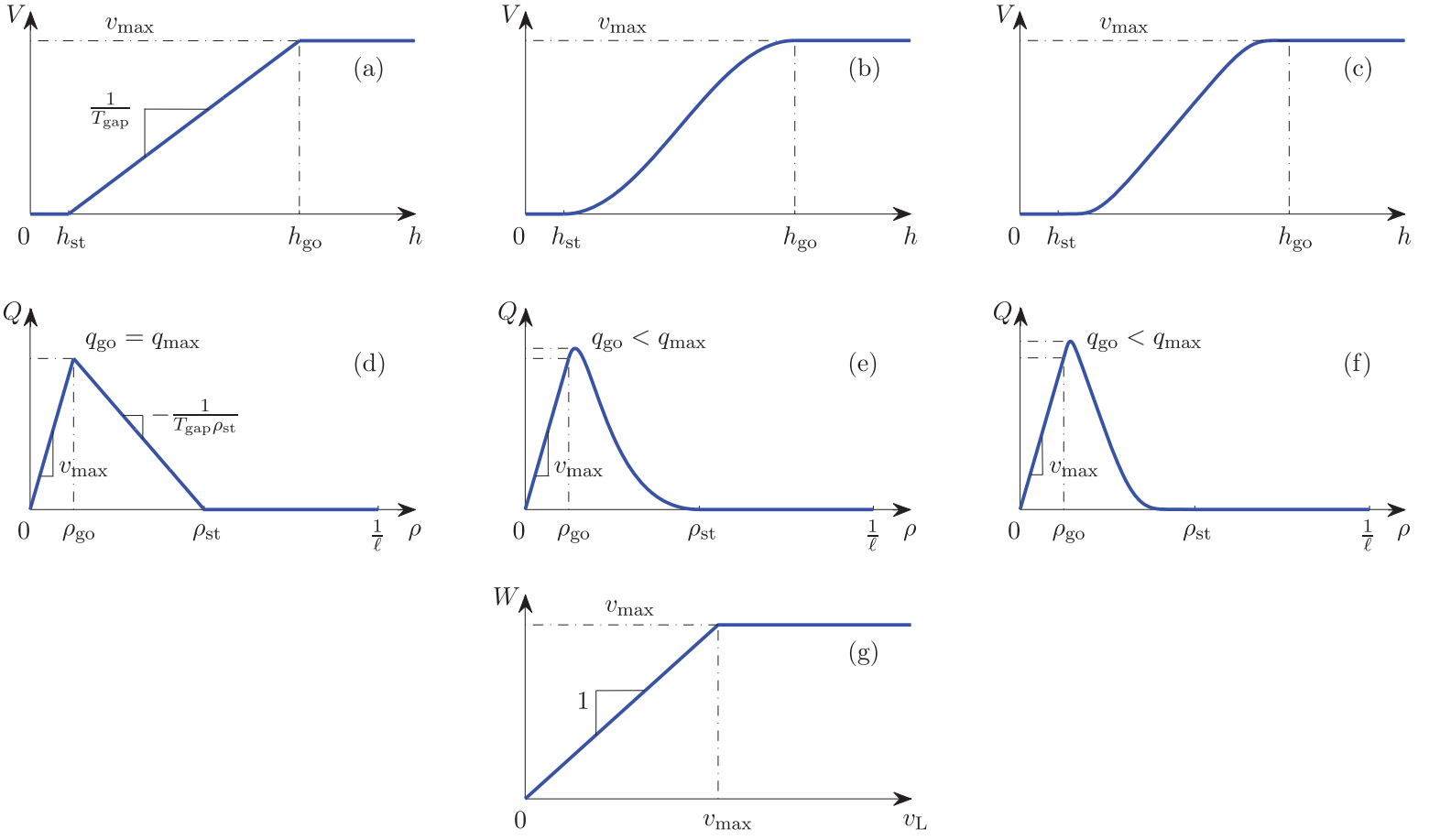

Figure 2. (a,b,c) Range policies (2) with the middle sections given by (3)–(5). (d)–(f) Fundamental diagrams corresponding to the range policies. (g) Saturation function (10).

for $j = 1, \ldots, n$. Here s and s_{L_j} denote the positions of the front bumper of the vehicles along the road while $v = \dot{s}$ and $v_{\mathrm{L}_j} = \dot{s}_{\mathrm{L}_j}$ are the corresponding velocities; see Figure 1. These positions, velocities, and accelerations can be obtained by global positioning systems (GPS), wheel-based sensors, and accelerometers.[3] Note that for accurate positioning differential GPS may be required. The symbols ℓ_{L_j} represent the lengths of the vehicles (not spelled out in Figure 1). The integral variables z_j are introduced to eliminate the steady-state error. Alternatively, one may use the headways $h = s_{\mathrm{L}_1} - s - \ell_{\mathrm{L}_1}$ and $h_{\mathrm{L}_j} = s_{\mathrm{L}_{j+1}} - s_{\mathrm{L}_j} - \ell_{\mathrm{L}_{j+1}}$ which yields

$$\dot{z}_j = V\left(\frac{1}{j}\left(h + \sum_{k=1}^{j-1} h_{\mathrm{L}_k}\right)\right) - v. \tag{9}$$

The controller is constructed such that the CCC vehicle intends to keep a velocity dependent distance (given by the range policy (2)) from the vehicle ahead and intends to keep multiples of this distance (minus the vehicle lengths) from the vehicles that are further ahead.[29,30] Moreover, the CCC vehicle also tries to match its speed and acceleration to the speed and acceleration of vehicles ahead. Thus, when the vehicles ahead travel with the same velocity v^* and they are equidistant with headways h^*, then the CCC vehicle can achieve the desired equilibrium $v^* = V(h^*)$. This equilibrium is independent of the external disturbances, the communication topology, the control gains, and the communication delays. The control law (7) also contains the saturation function

$$W(v_{\mathrm{L}_j}) = \begin{cases} v_{\mathrm{L}_j} & \text{if } v_{\mathrm{L}_j} \leq v_{\max}, \\ v_{\max} & \text{if } v_{\mathrm{L}_j} > v_{\max}, \end{cases} \tag{10}$$

shown in Figure 2(g), to hinder the CCC vehicle to follow vehicles whose velocity is larger than $v_{\max}$. The range policy (2) and the function (10) allow the controller to automatically switch between CCC and standard cruise control when other vehicles move away.

The proportional, integral, velocity, and acceleration gains are denoted by K_{p_j}, K_{i_j}, K_{v_j}, and K_{a_j}, respectively. When the CCC vehicle is not receiving messages from the jth vehicle ahead the corresponding gains are set to zero. Also, when the jth vehicle is not transmitting a certain type of information (e.g. acceleration) then the corresponding gain is set to zero. This way the CCC vehicles exploits all available information and the controller remains functional even when not all vehicles ahead are broadcasting.

We remark that apart from the nonlinearities arising in the vehicle dynamics (1) and the PIVA controller (7), (8) one may take into account the engine saturation.[31] In this case (6) shall be substituted by

$$T_{\mathrm{en}}(t) = U\left(\sum_{j=1}^{n} T_{\mathrm{com},j}(t - \sigma_j), v(t)\right), \tag{11}$$

where the function U saturates at the maximum available torque (which depends on the speed $v(t)$) and at the minimum available braking torque. These saturations do not effect the linear stability analysis but would make the nonlinear analysis more complex so these are neglected here.

2.3. Communication delays

When using wireless V2V communication, time delays appear in the control loop since messages have to be processed by both the sender and the receiver. First, the sender samples its kinematic properties (GPS location, wheel-based velocity) and after processing the information the broadcasting unit (DSRC radio) sends the packet using the broadcast-and-catch wireless protocol IEEE802.11p.[32] If the packet is successfully received by the receiver then the information is processed and the controller assigns the appropriate commands for the engine or brake torque. Indeed, each of these processes takes time and the sampling time is set such that it is larger than the sum of these processing times. Typically, $\Delta t = 100$ ms is used in current DSRC standards. We remark that according to the IEEE802.11p protocol, successful packet delivery is not acknowledged by the receiver and no packets are re-sent to be able to operate in dynamic traffic environments. For simplicity, we assume that the clocks of the vehicles are synchronised.

When all packets are delivered successfully, the use of a zero-order hold (ZOH) results in periodically varying time delays as shown in Figure 3(a). Thus, if the packet sent at $t = (k-1)\Delta t$ is successfully delivered, then it can be used by the CCC vehicle to set the torque at $t = k\Delta t$, which it kept constant until $t = (k+1)\Delta t$. This means that the delay in the control loop increases from Δt to $2\Delta t$ during the time interval $t \in [k\Delta t, (k+1)\Delta t)$, and then it drops back to Δt when a new packet is put in use at $t = (k+1)\Delta t$; see Figure 3(a) and [33]. However, when only every rth packet is delivered, the delay increases to $(r+1)\Delta t$ before dropping back to Δt; see Figure 3(b) and (c) for $r = 2$ and $r = 3$, respectively. Indeed, packet drops typically occur in a stochastic manner which results in stochastic delay variations as shown in Figure 3(d).

In this paper our goal is to understand the trends implied by the delay, and thus, we approximate the time-varying communication delays with their time average, denoted by σ_j in (6). In particular, when every rth packet is delivered, we have

$$\sigma = \frac{r+2}{2}\Delta t. \tag{12}$$

In the stochastic case we can use the mean of the delay distribution to approximate the average delay. Since packet delivery can be modelled by Bernoulli trials, we use the mean of the corresponding geometric distribution of the first success time to obtain the delay

$$\sigma = \frac{1}{p}\Delta t, \tag{13}$$

where p is the probability of successful packet delivery.

In Section 3 we analyse the stability of a simple predecessor–follower configuration using the average delay approximation. In order to validate of this approximation, we carry out the calculations with ZOH with no packet drops ($r = 1$ in (12) and Figure 3(a)) in Appendix 2. We demonstrate that the stability charts obtained with the two different methods are almost indistinguishable from each other. For deterministic packet drops ($r > 1$ in (12) and Figure 3(b),(c)) the ZOH calculations become much more complex while the complexity of average delay approximation remains the same. In this case the average delay approximation still gives a good approximation of the stability chart obtained using ZOH (though the difference is larger than with no packet drops). For stochastic packet drops

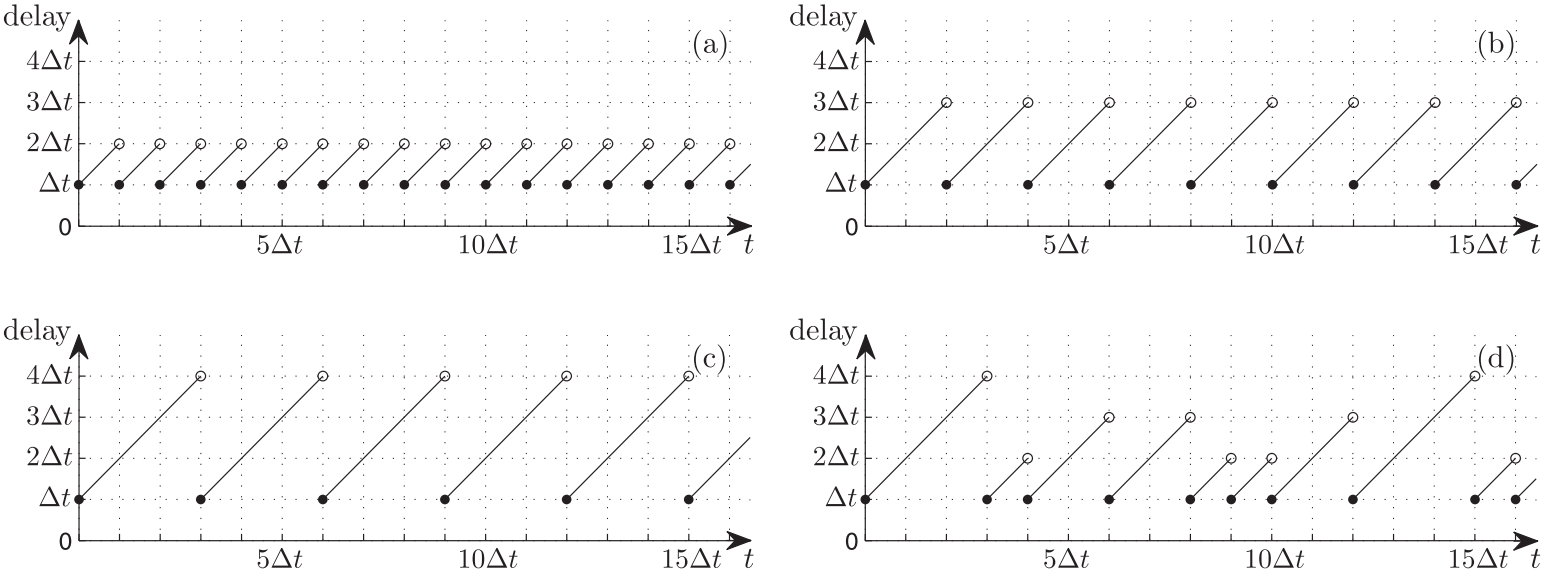

Figure 3. Time-varying communication delays when using a ZOH in the controller. (a) No packet loss. (b) Every second packet is received. (c) Every third packet is received. (d) Packets are lost in a stochastic manner.

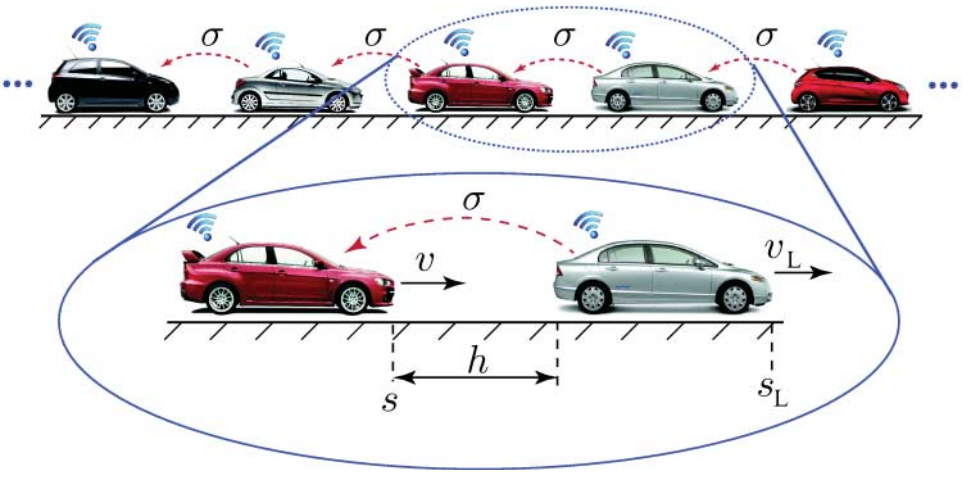

Figure 4. A CVS built as the concatenation of the simplest CCC configuration (zoomed).

(Figure 3(d)) using the average delay approximation (13) allows us to identify the tendencies, but more sophisticated methods are needed to obtain quantitative results. Taking the mean dynamics, the resulting distributed delay system can be used to obtain necessary stability conditions; see [16] with uniform distribution and [34] with geometric distribution. However, to be able to derive necessary and sufficient conditions one needs to analyse the covariance dynamics.[34]

2.4. Predecessor–follower configuration

When mixing CCC and non-CCC vehicles a large variety CVS may arise as discussed in [35] where simplified model and a simplified controller were used. Here we use the physics-based model and controller described above and we analyse the simplest CCC configuration where the CCC vehicle receives information from the vehicle immediately ahead. The concatenation of this setup gives rise to a simple CVS of predecessor–follower type; see Figure 4.

In this case (6)–(9) are simplified to

$$T_{\mathrm{en}}(t) = T_{\mathrm{com}}(t-\sigma), \tag{14}$$

where

$$T_{\mathrm{com}} = K_{\mathrm{p}}\dot{z} + K_{\mathrm{i}}z + K_{\mathrm{v}}(W(v_{\mathrm{L}}) - v) + K_{\mathrm{a}}\dot{v}_{\mathrm{L}}, \tag{15}$$

and

$$\dot{z} = V(h) - v, \tag{16}$$

where the index $j=1$ is dropped for simplicity. Inserting these into (1), and considering the simplification $\phi = 0$, $v_{\mathrm{w}} = 0$ and $J = 0 \Longrightarrow m_{\mathrm{eff}} = m$, the system can be described by

the delay differential equations

$$\begin{aligned}\dot{h}(t) &= v_{\mathrm{L}}(t) - v(t),\\ \dot{v}(t) &= -\gamma\, g - \frac{k}{m}v^2(t) + \hat{K}_{\mathrm{p}}\dot{z}(t-\sigma) + \hat{K}_{\mathrm{i}}z(t-\sigma)\\ &\quad + \hat{K}_{\mathrm{v}}(W(v_{\mathrm{L}}(t-\sigma)) - v(t-\sigma)) + \hat{K}_{\mathrm{a}}\dot{v}_{\mathrm{L}}(t-\sigma),\\ \dot{z}(t) &= V(h(t)) - v(t),\end{aligned} \tag{17}$$

where v_{L} is the input and v is the output and

$$\hat{K}_{\mathrm{p}} = \frac{K_{\mathrm{p}}\eta}{mR}, \quad \hat{K}_{\mathrm{i}} = \frac{K_{\mathrm{i}}\eta}{mR}, \quad \hat{K}_{\mathrm{v}} = \frac{K_{\mathrm{v}}\eta}{mR}, \quad \hat{K}_{\mathrm{a}} = \frac{K_{\mathrm{a}}\eta}{mR}. \tag{18}$$

Note that $\hat{K}_{\mathrm{p}}$ and $\hat{K}_{\mathrm{v}}$ have the unit [1/s], $\hat{K}_{\mathrm{i}}$ have the unit [1/s^2], and $\hat{K}_{\mathrm{p}}/\hat{K}_{\mathrm{i}}$ represents the characteristic time needed to make the steady-state error zero. Indeed, $\hat{K}_{\mathrm{a}}$ is a dimensionless quantity.

We remark that instead of (14) the first-order lag approximation

$$T_{\mathrm{com}}(t) = T_{\mathrm{en}}(t+\sigma) \approx T_{\mathrm{en}}(t) + \sigma\dot{T}_{\mathrm{en}}(t), \tag{19}$$

is often used in the literature; see Appendix 3. However, we will demonstrate in the next section that this only gives a good approximation of the dynamics for small gains and low frequencies.

3. Linear stability analysis and stability charts

In this section we analyse the linear stability of the simple model (17). In particular, we characterise the domains of plant stability and string stability in the parameter space $(\hat{K}_{\mathrm{p}}, \hat{K}_{\mathrm{i}}, \hat{K}_{\mathrm{v}}, \sigma)$. For simplicity, we consider $\hat{K}_{\mathrm{a}} = 0$ and refer the reader to [36] where the effects of this parameter are studied on a simplified model.

3.1. Linearisation and transfer function

When considering the constant input $v_{\mathrm{L}}(t) \equiv v_{\mathrm{L}}^*$, where $0 \le v_{\mathrm{L}}^* \le v_{\max}$, the system (17) possesses the equilibrium

$$v^* = v_{\mathrm{L}}^*, \quad v^* = V(h^*), \quad z^* = \frac{1}{\hat{K}_{\mathrm{i}}}\left(\gamma g + \frac{k}{m}(v^*)^2\right), \tag{20}$$

where the last equation determines the engine torque $T_{\mathrm{en}}^* = K_{\mathrm{i}}z^* = mR/\eta(\gamma g + k/m(v^*)^2)$ required to maintain the equilibrium. We remark that in the velocity range $0 < v_{\mathrm{L}}^* < v_{\max}$ the relationship $v^* = V(h^*)$ gives the unique headway $h^* = F^{-1}(v^*)$; see (2). On the other hand, for $v_{\mathrm{L}}^* = 0$ any $h^* \le h_{\mathrm{st}}$ is possible, and for $v_{\mathrm{L}}^* = v_{\max}$ any $h^* \ge h_{\mathrm{go}}$ is possible. Finally, for $v_{\mathrm{L}}^* > v_{\max}$ the state $v^* = v_{\max}$ can be achieved though this not an equilibrium of (17) since the left-hand side of the first equation is not zero. In this case, the follower simply operates in standard cruise control mode while the leader is getting away. In this paper we focus on the dynamic regime $0 < v_{\mathrm{L}}^* < v_{\max}$.

Defining the perturbations

$$x(t) = \begin{bmatrix} \tilde{h}(t) \\ \tilde{v}(t) \\ \tilde{z}(t) \end{bmatrix} = \begin{bmatrix} h(t) - h^* \\ v(t) - v^* \\ z(t) - z^* \end{bmatrix}, \quad u(t) = \tilde{v}_{\mathrm{L}}(t) = v_{\mathrm{L}}(t) - v^*, \tag{21}$$

the linearisation of (17) can be written as

$$\dot{x}(t) = \mathbf{A}\, x(t) + \mathbf{A}_\sigma\, x(t-\sigma) + \mathbf{B}\, u(t) + \mathbf{B}_\sigma\, u(t-\sigma), \tag{22}$$

with matrices

$$\mathbf{A} = \begin{bmatrix} 0 & -1 & 0 \\ 0 & -2\frac{k}{m}v^* & 0 \\ N_* & -1 & 0 \end{bmatrix}, \quad \mathbf{A}_\sigma = \begin{bmatrix} 0 & 0 & 0 \\ N_*\hat{K}_{\mathrm{p}} & -(\hat{K}_{\mathrm{p}} + \hat{K}_{\mathrm{v}}) & \hat{K}_{\mathrm{i}} \\ 0 & 0 & 0 \end{bmatrix},$$
$$\mathbf{B} = \begin{bmatrix} 1 \\ 0 \\ 0 \end{bmatrix}, \quad \mathbf{B}_\sigma = \begin{bmatrix} 0 \\ \hat{K}_{\mathrm{v}} \\ 0 \end{bmatrix}. \tag{23}$$

Here the symbol N_* represents the derivative of the range policy (2) at the equilibrium headway h^* that can be expressed as

$$N_* = V'(h^*) = \begin{cases} 0 & \text{if } h^* \le h_{\mathrm{st}}, \\ F'(h^*) & \text{if } h_{\mathrm{st}} < h^* < h_{\mathrm{go}}, \\ 0 & \text{if } h^* \ge h_{\mathrm{go}}, \end{cases} \tag{24}$$

which is equivalent to

$$N_* = F'(F^{-1}(v^*)), \tag{25}$$

for $0 < v^* < v_{\max}$. For the range policy (3) we obtain

$$N_* \equiv \frac{v_{\max}}{h_{\mathrm{go}} - h_{\mathrm{st}}}, \tag{26}$$

while for (4) we have

$$N_* = \pi \frac{v_{\max}}{h_{\mathrm{go}} - h_{\mathrm{st}}} \sqrt{\frac{v^*}{v_{\max}} \left(1 - \frac{v^*}{v_{\max}}\right)}, \tag{27}$$

and these are plotted in Figure 5(a) and (b), respectively. For the range policy (5) the algebraic expression becomes complicated but the function looks similar to case (4) and both functions reach their maximum at $v^* = v_{\max}/2$ where we have $N^* = \pi/2 \cdot v_{\max}/(h_{\mathrm{go}} - h_{\mathrm{st}})$. Notice that N_* has the unit [1/s]. Thus, for $0 < v^* < v_{\max}$, we may define the effective time gap as

$$T_{\mathrm{gap}} = \frac{1}{N_*}. \tag{28}$$

This is constant in case of the range policy (3) but changes with velocity v^* for range policies (4) and (5).

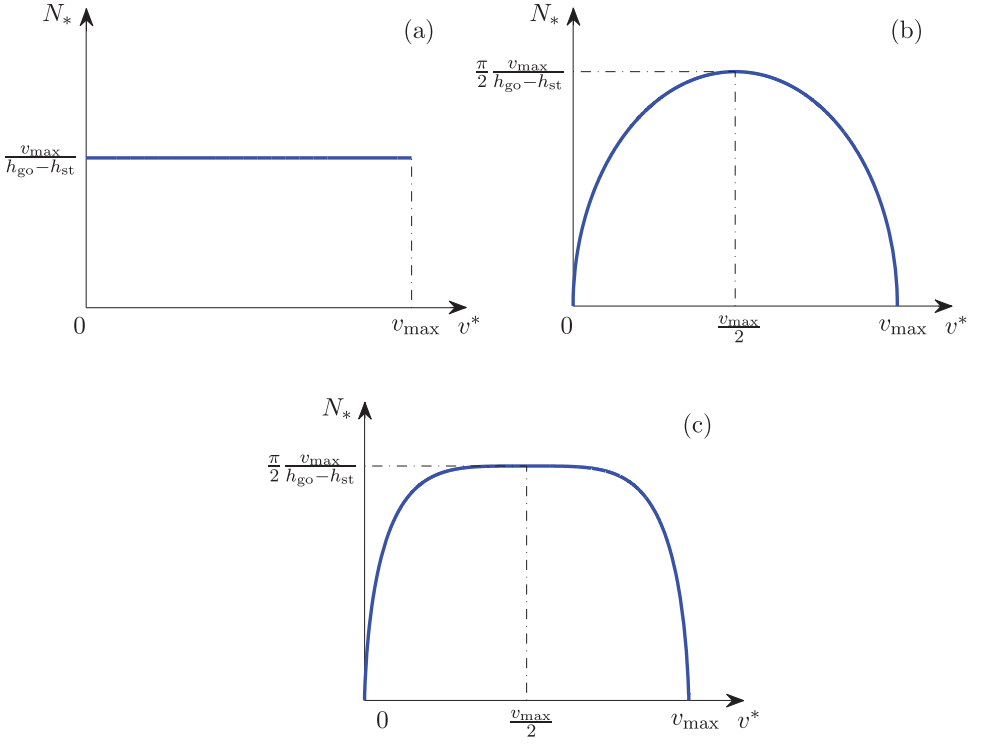

Figure 5. The derivative (25) of the range policy as a function of the equilibrium velocity v^*. Panels (a), (b), and (c) correspond to (3),(4), and (5), respectively.

The output $y(t) = \tilde{v}(t) = v(t) - v^*$ can be formally written as

$$y(t) = \mathbf{C}\,x(t) + \mathbf{C}_\sigma\,x(t-\sigma) + \mathbf{D}\,u(t) + \mathbf{D}_\sigma\,u(t-\sigma), \tag{29}$$

with matrices

$$\mathbf{C} = \begin{bmatrix} 0 & 1 & 0 \end{bmatrix}, \quad \mathbf{C}_\sigma = \begin{bmatrix} 0 & 0 & 0 \end{bmatrix}, \quad \mathbf{D} = \mathbf{D}_\sigma = 0. \tag{30}$$

Taking the Laplace transform of (22) and (29) with zero initial conditions on the interval $t \in [-\sigma, 0]$ and using the matrices (23) and (30) result in the transfer function

$$\begin{aligned} \Gamma(s) = \frac{\tilde{V}(s)}{\tilde{V}_{\mathrm{L}}(s)} &= (\mathbf{C} + \mathbf{C}_\sigma \mathrm{e}^{-s\sigma})(s\mathbf{I} - \mathbf{A} - \mathbf{A}_\sigma \mathrm{e}^{-s\sigma})^{-1}(\mathbf{B} + \mathbf{B}_\sigma \mathrm{e}^{-s\sigma}) + (\mathbf{D} + \mathbf{D}_\sigma \mathrm{e}^{-s\sigma}) \\ &= \frac{\hat{K}_{\mathrm{v}} s^2 + N_* \hat{K}_{\mathrm{p}} s + N_* \hat{K}_{\mathrm{i}}}{(s^3 + 2\frac{k}{m} v^* s^2)\mathrm{e}^{s\sigma} + (\hat{K}_{\mathrm{p}} + \hat{K}_{\mathrm{v}})s^2 + (N_* \hat{K}_{\mathrm{p}} + \hat{K}_{\mathrm{i}})s + N_* \hat{K}_{\mathrm{i}}}, \end{aligned} \tag{31}$$

where $\tilde{V}(s)$ and $\tilde{V}_{\mathrm{L}}(s)$ denote the Laplace transform of $\tilde{v}(t)$ and $\tilde{v}_{\mathrm{L}}(t)$, respectively.

We remark that the transfer function of the system with the first-order lag approximation (19) can be obtained by standard analysis of the corresponding ordinary differential equations; see Appendix 3. This corresponds to the approximation $\mathrm{e}^{s\sigma} \approx 1 + \sigma s$ in (31). Again, we emphasise that this only provides reliable stability results for small gains and low frequencies as will be shown below.

3.2. Plant stability

Here we investigate the dynamics in the vicinity of the equilibrium (20) at the linear level by using the system (22), (29), and the corresponding transfer function (31). We summarise the results using stability charts in the $(\hat{K}_\mathrm{i}, \hat{K}_\mathrm{p})$-plane and in the $(\hat{K}_\mathrm{v}, \hat{K}_\mathrm{p})$-plane for different values of the delay σ. In this subsection we study plant stability which means that if the leader is driving with constant speed the CCC vehicle approaches this speed. In the next subsection we investigate string stability which means that if the speed of the vehicle ahead varies, these fluctuations are attenuated by the CCC vehicle. That is, string stability implies that fluctuations decay as they propagate backward along the chain of CCC vehicles in Figure 4. We show the results for $v^* = 15$ [m/s] (that is, $h^* = 20$ [m]) using the parameters in Table A1. These result in $N_* = \pi/2$ [1/s], that is, $T_\mathrm{gap} = 2/\pi \approx 0.64$ [s] for the range policies (2), (4) and (2), (5); see Figure 5(b) and (c). As will be shown below this gives the worst-case scenario in terms of plant and string stability.

To achieve plant stability, all the infinitely many poles of the transfer function (31) have to be located in the left-half complex plane. To ensure this, we analyse the characteristic equation obtained by setting the denominator of the transfer function (31) to be zero. For $s = 0$, we obtain the plant stability boundary

$$\hat{K}_\mathrm{i} = 0. \tag{32}$$

When crossing this stability boundary a real characteristic root crosses the imaginary axis in the complex plane and the system diverges from the equilibrium in a non-oscillatory way.

Moreover, substituting $s = \mathrm{i}\Omega$, $\mathrm{i}^2 = -1$, $\Omega > 0$ into the characteristic equation, separating the real and imaginary parts, algebraic manipulations lead to

$$\begin{aligned}
\hat{K}_\mathrm{p} &= -2\frac{k}{m}v^* \cos(\Omega\sigma) + \Omega \sin(\Omega\sigma) - \hat{K}_\mathrm{v} + \frac{N_* \hat{K}_\mathrm{i}}{\Omega^2}, \\
\hat{K}_\mathrm{i} &= \frac{\Omega^2}{N_*^2 + \Omega^2}\left(\left(2\frac{k}{m}v^* N_* + \Omega^2\right)\cos(\Omega\sigma) - \left(N_* - 2\frac{k}{m}v^*\right)\Omega \sin(\Omega\sigma) + N_* \hat{K}_\mathrm{v}\right).
\end{aligned} \tag{33}$$

This gives the stability boundary in the $(\hat{K}_\mathrm{p}, \hat{K}_\mathrm{i})$ parameter plane as shown by the solid red curve in Figure 6(a) for $\hat{K}_\mathrm{v} = 0.5$ [1/s] and $\sigma = 0.2$ [s]. (This σ value corresponds to the scenario when every second packet is delivered; cf. (12) and Figure 3(b).) When crossing the stability boundary (33), a pair of complex conjugate roots crosses the imaginary axis at $\pm\mathrm{i}\Omega$ and oscillations arise with frequency close to Ω. This frequency increases along the boundary as shown in Figure 6(b) resulting in low- and high- frequency oscillations when crossing the lower and the upper part of the plant stability boundary, respectively. By applying Stépán's formulae,[37] it can be proven that plant stability is guaranteed within the lobe-shaped area enclosed by (32) and (33) as shown by the union of the light and dark grey areas.

The stability losses are demonstrated by plotting the leading eigenvalues in the complex plane in Figure 6(c)–(h) for the points marked A, B, C, G, H, I in Figure 6(a) at $\hat{K}_\mathrm{i} = 0.5$ [1/s^2]. The eigenvalues are calculated by using the software DDE-biftool.[38] Cases G, H, I represent a low-frequency stability loss ($\Omega \approx 1.07$ [1/s] in case G) where a pair of roots

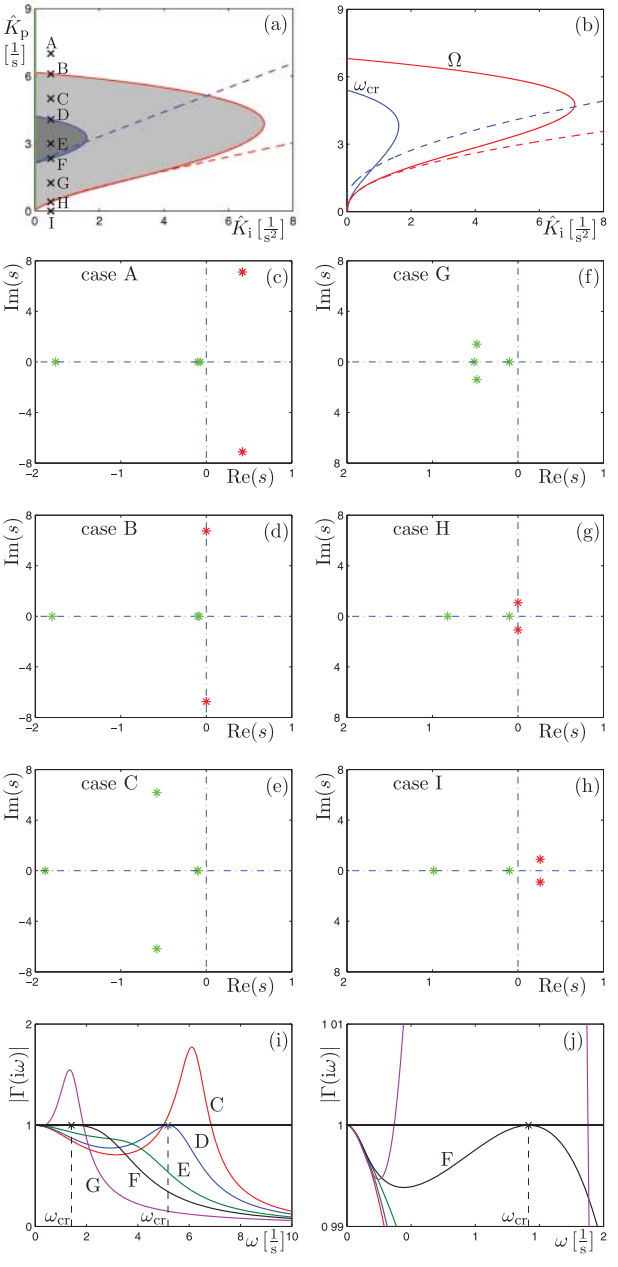

Figure 6. (a) Stability diagram in the $(\hat{K}_i, \hat{K}_p)$ parameter plane for $\hat{K}_v = 0.5$ [1/s] and $\sigma = 0.2$ [s]. The plant and string stability boundaries are shown as solid red and solid blue curves, respectively, while the dashed curves correspond to the first-order lag approximation. The green vertical line (close to the vertical axis) is a string stability boundary with $\omega_{cr} = 0$. Shading indicates plant stability while string stability is only satisfied in the dark grey region. (b) Variation of the frequencies Ω and ω_{cr} along the plant and string stability boundaries. (c)–(h) Eigenvalue plots for the points A, B, C, G, H, I marked in panel (a). (i), (j) Amplification ratios as a function of the excitation frequency for points C, D, E, F, G marked in panel (a).

moves to the right-hand side as $\hat{K}_\mathrm{p}$ is decreased. On the other hand, Cases A, B, C represent a high-frequency stability loss ($\Omega \approx 6.74[1/s]$ in case B) where a pair of roots crosses the imaginary axis as $\hat{K}_\mathrm{p}$ is increased.

We remark that one may derive plant stability boundaries for the system with the first-order lag approximation (19) by using the transfer function (61) given in Appendix 3 and the results are depicted as red dashed curves in Figure 6(a), (b). These only approximate the stability boundaries well for low frequencies and small gains. In fact, the first-order lag approximation predicts a much larger plant stable area (above the red dashed curve in Figure 6(a)) compared to the shaded domain. In particular, the approximation would allow the use of high gains while these lead to high-frequency oscillations in the delayed system.

3.3. String stability

To determine string stability (attenuation of fluctuations) at the linear level we use the Fourier decomposition of the signal $v_\mathrm{L}(t)$. As superposition holds for linear systems, string stability can be guaranteed by ensuring that the output–input amplitude ratio stays below 1 for all excitation frequencies. In particular, driving the system with the sinusoidal input

$$v_\mathrm{L}(t) = v_\mathrm{L}^* + \tilde{v}_\mathrm{L}(t) = v_\mathrm{L}^* + v_\mathrm{L}^\mathrm{amp} \sin(\omega t), \tag{34}$$

results in the steady-state output

$$v^\mathrm{ss}(t) = v^* + \tilde{v}(t) = v^* + v_\mathrm{L}^\mathrm{amp} |\Gamma(\mathrm{i}\omega)| \sin(\omega t + \angle\Gamma(\mathrm{i}\omega)), \tag{35}$$

where $v^* = v_\mathrm{L}^*$ (cf. 20), while $\Gamma(\mathrm{i}\omega)$ is obtained from the transfer function (31). Here $|\cdot|$ and $\angle\cdot$ denote the magnitude and angle of a complex number, respectively. That is, string stability is satisfied when

$$|\Gamma(\mathrm{i}\omega)| < 1, \tag{36}$$

for all $\omega > 0$. Using (31) and some algebraic manipulations this condition can be re-written as

$$\begin{aligned} G(\omega) = &-\omega^4 - \left(\hat{K}_\mathrm{p}^2 + 2\hat{K}_\mathrm{p}\hat{K}_\mathrm{v} + 4\frac{k^2}{m^2}(v^*)^2\right)\omega^2 - \hat{K}_\mathrm{i}^2 \\ &+ 2\left(\left(\left(N_* - 2\frac{k}{m}v^*\right)\hat{K}_\mathrm{p} + \hat{K}_\mathrm{i} - 2\frac{k}{m}v^*\hat{K}_\mathrm{v}\right)\omega^2 + 2\frac{k}{m}v^*N_*\hat{K}_\mathrm{i}\right)\cos(\omega\sigma) \\ &+ 2\left(\left(\hat{K}_\mathrm{p} + \hat{K}_\mathrm{v}\right)\omega^2 + 2\frac{k}{m}v^*N_*\hat{K}_\mathrm{p} - \left(N_* - 2\frac{k}{m}v^*\right)\hat{K}_\mathrm{i}\right)\omega\sin(\omega\sigma) < 0, \end{aligned} \tag{37}$$

for all $\omega > 0$ which is satisfied if the maximum of $G(\omega)$ is smaller than zero. Indeed, G depends on many other parameters, including the control gains $\hat{K}_\mathrm{p}$, $\hat{K}_\mathrm{i}$, $\hat{K}_\mathrm{v}$, but these are not spelled out for the sake of simplicity.

If G reaches its maximum at $\omega_\mathrm{cr} = 0$, then the stability condition simplifies to

$$\hat{K}_\mathrm{i} > 4\frac{k}{m}v^*N_*, \tag{38}$$

and the corresponding boundary is shown in Figure 6(a) as a green vertical line (close to the vertical axis). On the other hand, if G reaches its maximum at $\omega_\mathrm{cr} > 0$, then the stability

boundary is given by

$$\begin{aligned} G(\omega_{\mathrm{cr}}) &= 0, \\ H(\omega_{\mathrm{cr}}) &= \frac{\partial G}{\partial \omega_{\mathrm{cr}}} = 0, \end{aligned} \tag{39}$$

where the condition $(\partial^2 G/\partial \omega_{\mathrm{cr}}^2) < 0$ also has to be satisfied. However, (39) cannot be solved explicitly for the gain parameters. In order to derive the stability boundaries in the parametric form $(\hat{K}_{\mathrm{p}}(\omega_{\mathrm{cr}}), \hat{K}_{\mathrm{i}}(\omega_{\mathrm{cr}}))$ we set up the mock ordinary differential equation

$$\begin{aligned} \frac{\mathrm{d}}{\mathrm{d}t}\hat{K}_{\mathrm{p}} &= G(\hat{K}_{\mathrm{p}}, \hat{K}_{\mathrm{i}}; \omega_{\mathrm{cr}}), \\ \frac{\mathrm{d}}{\mathrm{d}t}\hat{K}_{\mathrm{i}} &= H(\hat{K}_{\mathrm{p}}, \hat{K}_{\mathrm{i}}; \omega_{\mathrm{cr}}), \end{aligned} \tag{40}$$

and solve for its equilibrium while varying the parameter ω_{cr} by applying numerical continuation.[39] This requires an initial guess of the solution for a particular value of ω_{cr} that can be corrected using the Newton–Raphson method. Then the corrected solution can be used as an initial guess for nearby ω_{cr} values. This way the stability boundary can be continued while ω_{cr} is varied.

The corresponding string stability boundary is shown as a blue solid curve in Figure 6(a) for $\hat{K}_{\mathrm{v}} = 0.5$ [1/s] and $\sigma = 0.2$ [s] while the corresponding frequencies ω_{cr} are plotted in Figure 6(b). The lobe-shaped dark grey domain enclosed by (38) and the solution of (39) corresponds to string stable parameter combinations. Notice that ω_{cr} increases along the boundary. This means that string stability occurs for low- and high- frequencies when crossing the stability boundary for low and high values of $\hat{K}_{\mathrm{p}}$, respectively. We remark that there exist other string stability boundaries that are located in the plant unstable (white) domain. These are not shown in the figure since they have no physical meaning.

In order to demonstrate the string stability losses at different frequencies we plot the amplification ratio $|\Gamma(\mathrm{i}\omega)|$ as a function of the frequency ω in Figure 6(i), (j) for the points marked C, D, E, F, G in Figure 6(a) at $\hat{K}_{\mathrm{i}} = 0.5$ [1/s^2]. Cases E, F, G show a low-frequency string stability loss that occurs when $\hat{K}_{\mathrm{p}}$ is decreased. In particular, $\omega_{\mathrm{cr}} = 1.42$ [1/s] in case F (see the zoomed version in panel (j)), and thus, case G is string unstable in the frequency domain $\omega \in [0.37,\ 1.88]$ [1/s]. On the other hand, cases C, D, E correspond to a high-frequency string stability loss through the increase of $\hat{K}_{\mathrm{p}}$. Here we have $\omega_{\mathrm{cr}} = 5.17$ [1/s] in case D, and thus case C shows string unstable behaviour in the frequency domain $\omega \in [5.00,\ 6.86]$ [1/s].

Again, the string stability boundaries can be obtained numerically when using the first-order lag approximation (19) and the transfer function (61) given in Appendix 3. The results are plotted in Figure 6(a), (b) as blue dashed curves that only provide a good approximation of the stability boundaries for low frequencies and small gains. Also, the predicted string stable domain (above the blue dashed curve in Figure 6(a)) is significantly larger than the dark grey domain.

We demonstrate how the plant and string stable domains change with the communication delay σ in Figure 7 for $\hat{K}_{\mathrm{v}} = 0.5$ [1/s] where the same notation is used as in Figure 6(a), (b). For reference, we show the case when $\sigma = 0$ in Figure 7(a), (b). In this case selecting sufficiently large gains, (i.e., $\hat{K}_{\mathrm{p}} \gtrsim 2.13$ [1/s] and $\hat{K}_{\mathrm{i}} \gtrsim 0.0281$ [1/s^2]) ensures both plant and

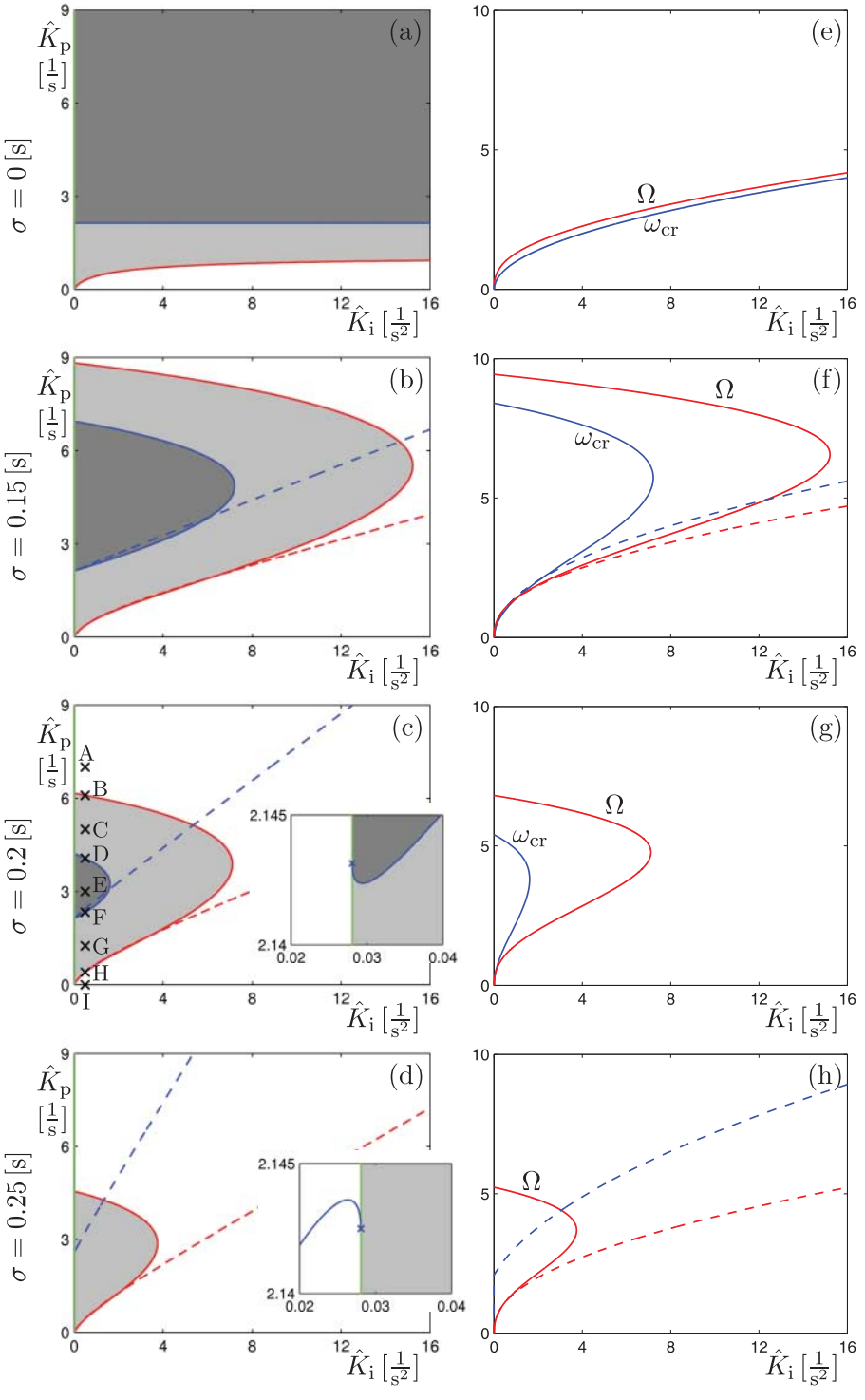

Figure 7. (a)–(d) Stability diagram in the $(\hat{K}_i, \hat{K}_p)$ parameter plane in case of $\hat{K}_v = 0.5$ [1/s] for different values of the communication delay σ as indicated. (e)–(g) Variation of the frequencies Ω and ω_{cr} along the plant and string stability boundaries. The same notation is used as in Figure 6(a), (b).

string stability. However, this does not hold for nonzero delay as shown in Figure 7(b)–(d), (f)–(h) where the σ values are selected according to (12) for $r = 1,2,3$. As the delay increases the stable domains shrink and for $\sigma = 0.25$ [s] the string stable domain disappears.

In order to show the effects caused by the variations of the gain parameter $\hat{K}_\mathrm{v}$, we fix $\hat{K}_\mathrm{i} = 0.5$ [1/s^2] and plot the plant and string stability boundaries in the $(\hat{K}_\mathrm{v}, \hat{K}_\mathrm{p})$-plane for different values of σ in Figure 8. In this case the plant stability boundary can be found in parametric form by rearranging (33) while the string stability boundary can be obtained by setting up a mock differential equation for $\hat{K}_\mathrm{p}$ and $\hat{K}_\mathrm{v}$, similar to (40). Notice that, apart from the zero delay case shown in Figure 8(a), (e), $\hat{K}_\mathrm{v}$ has to be between bounds in order to maintain stability. Figure 8(a)–(d) also illustrates that the plant and string stable domains shrink as the delay increases and that string stability is not possible to obtain when the delay exceeds some critical value. In particular, Figure 8(d), (h) depicts a scenario where the delay is very close to the critical value.

We remark that with no packet drops the stability results obtained above match very well with those obtained using ZOH in Appendix 2; compare Figure 7(b) with Figure A1(a) and Figure 8(b) with Figure A1(b). Moreover, when considering the general CCC setup in Figure 4 one may compare the speed variations of the CCC vehicle to any of the n vehicles ahead and obtain different string stability results.[35,36]

3.4. Calculating the critical delay

In order to obtain a performance limit of the controllers, here we determine the critical value of the delay beyond which no string stability is possible for any combination of the gain parameters $\hat{K}_\mathrm{p}, \hat{K}_\mathrm{i}, \hat{K}_\mathrm{v}$. By observing the zoomed inlets in Figure 7(c), (d) one may notice that the string stability boundary emanates for the $\omega_\mathrm{cr} = 0$ point (blue cross) in different ways. To characterise this behaviour we calculate the Taylor expansion of the stability boundary $(\hat{K}_\mathrm{p}(\omega_\mathrm{cr}), \hat{K}_\mathrm{i}(\omega_\mathrm{cr}))$ about $\omega_\mathrm{cr} = 0$:

$$\begin{aligned}\hat{K}_\mathrm{p}(\omega_\mathrm{cr}) &= \hat{K}_\mathrm{p}(0) + \left.\frac{\mathrm{d}\hat{K}_\mathrm{p}}{\mathrm{d}\omega_\mathrm{cr}}\right|_0 \omega_\mathrm{cr} + \left.\frac{1}{2}\frac{\mathrm{d}^2\hat{K}_\mathrm{p}}{\mathrm{d}\omega_\mathrm{cr}^2}\right|_0 \omega_\mathrm{cr}^2 + \cdots,\\ \hat{K}_\mathrm{i}(\omega_\mathrm{cr}) &= \hat{K}_\mathrm{i}(0) + \left.\frac{\mathrm{d}\hat{K}_\mathrm{i}}{\mathrm{d}\omega_\mathrm{cr}}\right|_0 \omega_\mathrm{cr} + \left.\frac{1}{2}\frac{\mathrm{d}^2\hat{K}_\mathrm{i}}{\mathrm{d}\omega_\mathrm{cr}^2}\right|_0 \omega_\mathrm{cr}^2 + \cdots,\end{aligned} \tag{41}$$

where the coefficients can be obtained by taking the total derivatives of functions $G(\hat{K}_\mathrm{p}(\omega_\mathrm{cr}), \hat{K}_\mathrm{i}(\omega_\mathrm{cr}), \omega_\mathrm{cr})$ and $H(\hat{K}_\mathrm{p}(\omega_\mathrm{cr}), \hat{K}_\mathrm{i}(\omega_\mathrm{cr}), \omega_\mathrm{cr})$ in (39) with respect to ω_cr. In particular, we obtain

$$\left.\frac{\mathrm{d}\hat{K}_\mathrm{p}}{\mathrm{d}\omega_\mathrm{cr}}\right|_0 = \left.\frac{\mathrm{d}\hat{K}_\mathrm{i}}{\mathrm{d}\omega_\mathrm{cr}}\right|_0 = \left.\frac{\mathrm{d}^2\hat{K}_\mathrm{i}}{\mathrm{d}\omega_\mathrm{cr}^2}\right|_0 = 0, \quad \left.\frac{\mathrm{d}^2\hat{K}_\mathrm{i}}{\mathrm{d}\omega_\mathrm{cr}^2}\right|_0 = -\left.\frac{\partial^2 G}{\partial\omega_\mathrm{cr}^2}\right|_0 \left(\left.\frac{\partial G}{\partial\hat{K}_\mathrm{p}}\right|_0\right)^{-1}. \tag{42}$$

Thus, solving $\mathrm{d}^2\hat{K}_\mathrm{i}/\mathrm{d}\omega_\mathrm{cr}^2|_0 = 0$ for σ one may obtain the critical delay where the stability boundary changes direction. In the general case it is difficult to calculate this σ analytically. To get some insight, first we consider $k/m = 0$ as this is a small number compared to any other constants in the systems; cf. Table A1 in Appendix 1.

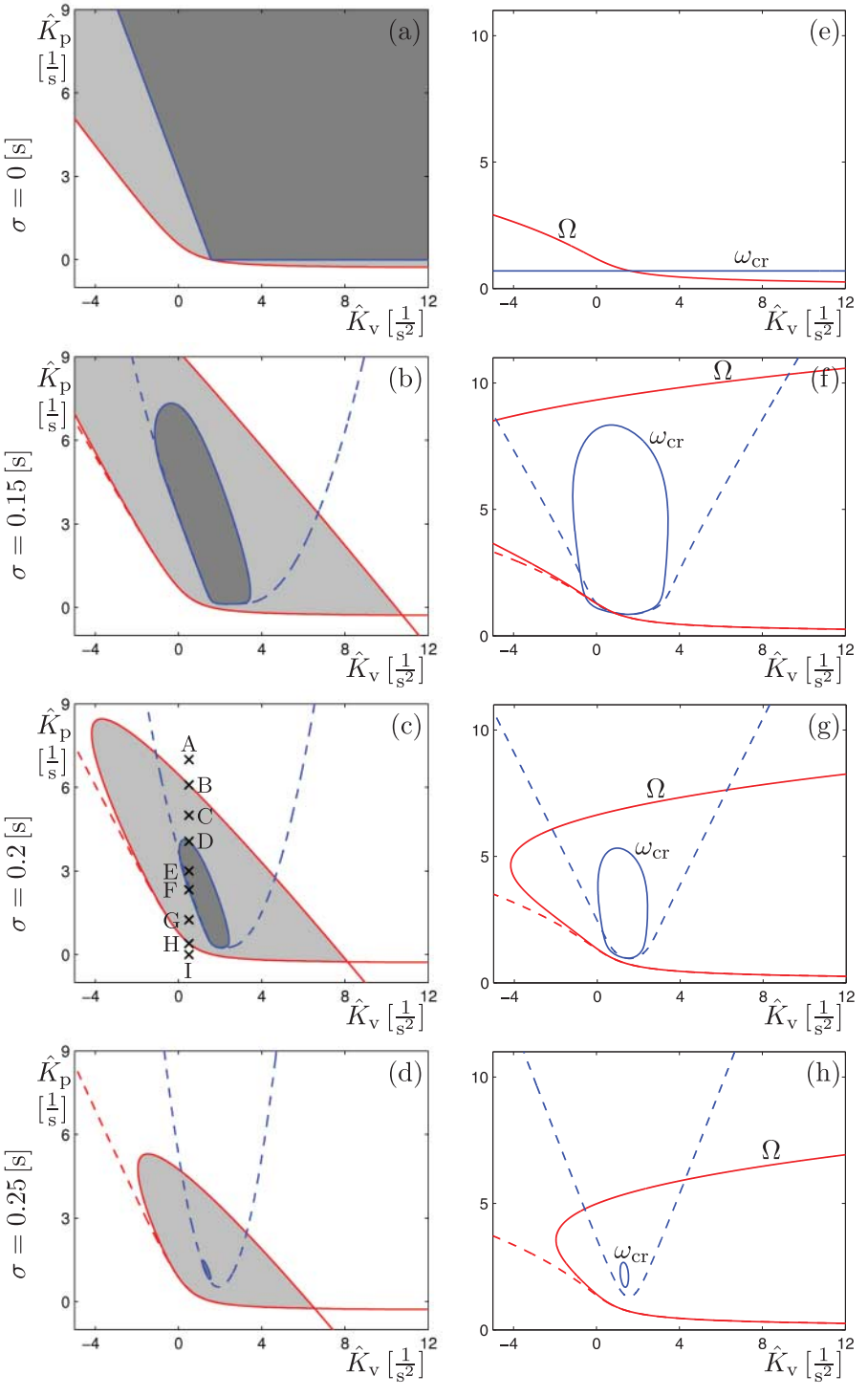

Figure 8. (a)–(d) Stability diagrams in the $(\hat{K}_\mathrm{v}, \hat{K}_\mathrm{p})$ parameter plane in case of $\hat{K}_\mathrm{i} = 0.5\,[1/\mathrm{s}^2]$ for different values of the delay σ as indicated. (e)–(g) Variation of the frequencies Ω and ω_cr along the plant and string stability boundaries. The same notation is used as in Figure 6(a), (b).

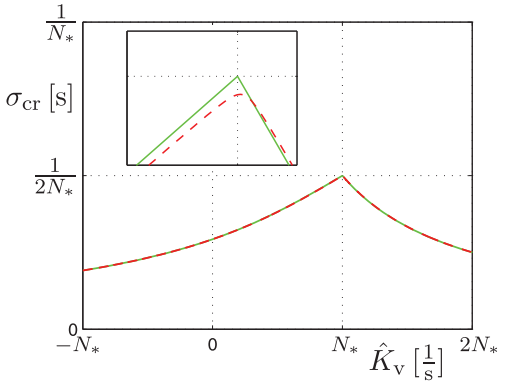

Figure 9. The critical delay $\sigma_{\rm cr}$ as the function of the gain parameter $\hat{K}_{\rm v}$. Solid green and red dashed curves are for $k/m = 0$ and $k/m = 2.9775 \cdot 10^{-4}$ [1/m], cf. Table. A1.

In this case we have

$$\left\{\begin{array}{l} \hat{K}_{\rm i}(0) = 0, \\ \hat{K}_{\rm p}(0) = 2(N_* - \hat{K}_{\rm v}), \\ \left.\dfrac{{\rm d}^2\hat{K}_{\rm i}}{{\rm d}\omega_{\rm cr}^2}\right|_0 = 2\dfrac{2N_*(N_* - \hat{K}_{\rm v})\sigma^2 - 2(2N_* - \hat{K}_{\rm v})\sigma + 1}{N_* - \hat{K}_{\rm v}}, \end{array}\right\} \quad \text{if } \hat{K}_{\rm v} \le N_*,$$

$$\left\{\begin{array}{l} \hat{K}_{\rm i}(0) = 0, \\ \hat{K}_{\rm p}(0) = 0, \\ \left.\dfrac{{\rm d}^2\hat{K}_{\rm i}}{{\rm d}\omega_{\rm cr}^2}\right|_0 = 2\dfrac{2\hat{K}_{\rm v}\sigma - 1}{\hat{K}_{\rm v} - N_*}, \end{array}\right\} \quad \text{if } \hat{K}_{\rm v} > N_*. \tag{43}$$

That is, solving ${\rm d}^2\hat{K}_{\rm i}/{\rm d}\omega_{\rm cr}^2|_0 = 0$, we obtain the critical delay

$$\sigma_{\rm cr} = \left\{\begin{array}{ll} \dfrac{2N_* - \hat{K}_{\rm v} - \sqrt{2N_*^2 - 2N_*\hat{K}_{\rm v} + \hat{K}_{\rm v}^2}}{2N_*(N_* - \hat{K}_{\rm v})} & \text{if } \hat{K}_{\rm v} \le N_*, \\ \dfrac{1}{2\hat{K}_{\rm v}} & \text{if } \hat{K}_{\rm v} > N_*, \end{array}\right. \tag{44}$$

which is shown in Figure 9 as a green solid curve.

Notice that $\sigma_{\rm cr}$ takes its maximum at $\hat{K}_{\rm v} = N_*$ where

$$\bar{\sigma}_{\rm cr} = \frac{1}{2N_*} = \frac{T_{\rm gap}}{2}, \tag{45}$$

cf. (28). This means that when delay is larger than the half of the time headway, there exist no combination of the gain parameters $\hat{K}_{\rm p}$, $\hat{K}_{\rm i}$, $\hat{K}_{\rm v}$ that can guarantee plant and string stability. When considering $k/m > 0$ the algebraic formulae become more complicated but one can calculate $\sigma_{\rm cr}$ numerically for different values of $\hat{K}_{\rm v}$ as shown in Figure 9 by the red dashed curve (that almost overlaps the green curve). The maximum still occurs at $\hat{K}_{\rm v} \approx N_*$, that is, $\bar{\sigma}_{\rm cr} \approx 1/2N_*$ as depicted by the zoomed version (shown as an inlet).

Similar arguments may be used when considering first-order lag approximation (19) and the transfer function (61). However, in this case there exist a boundary that leads to string stability even for $\sigma > \bar{\sigma}_{\rm cr}$; see the domains above the blue dashed curves in Figures 7(d) and 8(d).

4. Nonlinear effects

Since the vehicle model (1) as a well as the controller (6), (7), (9) are nonlinear, the question arises that how such nonlinearities influence the dynamics of CVS. Here we consider the predecessor–follower configuration studied in the previous section and investigate the effects of the nonlinear PIVA controller (14)–(16).

Regarding plant stability, we found that the linear stability losses detected above correspond to supercritical Hopf bifurcations at the nonlinear level [37,40] and self-excited oscillations appear outside the linearly stable domain only. That is, linear plant stability ensures global plant stability. In order to study string stability at the nonlinear level, we concatenate the system (17) and investigate the propagation of perturbations along the chain of 85+1 vehicles (see Figure 4) while using the range policy (2), (4) with parameters in Table A1. We show below that there exist parameter domains where the system is linearly string stable but it is string unstable at the nonlinear level. That is, small perturbations decay as they propagate along the platoon while large perturbations are amplified.

The results are summarised in Figure 10 for $\hat{K}_{\rm v} = 0.5$ [1/s], $\hat{K}_{\rm i} = 0.5$ [1/s^2], and $\sigma = 0.2$ [s]. In this case, $v^* = 15$ [m/s] corresponds to Figures 6(a), 7(c), and 9(c). Due to the nonlinear relationship (27) shown in Figure 5(b) we obtain the plant and string stability curves (red and blue) in the $(v^*, \hat{K}_{\rm p})$-plane as shown in Figure 10(a). The corresponding critical frequencies are plotted in Figure 10(b). In order to demonstrate the nonlinear effects we select the parameters corresponding to the point J located in the linearly string stable domain in Figure 10(a), that is, we consider $v^* = 25$ [m/s] and $\hat{K}_{\rm p} = 1.6$ [1/s].

We set the velocity of the head vehicle (the first vehicle in the platoon) to be

$$v_{\rm H}(t) = v_{\rm H}^* + v_{\rm H}^{\rm amp} \sin(\omega t), \tag{46}$$

cf. (34) and vary the amplitude $v_{\rm H}^{\rm amp}$ and the frequency ω. In steady state the velocity of the tail vehicle becomes

$$v_{\rm T}^{\rm ss}(t) = v_{\rm T}^{\rm amp} \phi(t), \tag{47}$$

where $\phi(t)$ is a $2\pi/\omega$-periodic function with amplitude 1. (This form may not hold for a general system but we found it to be true for the type of nonlinearities used here.) We use the numerical continuation package DDE-biftool [38] to compute the steady-state oscillations. Since this package can only handle autonomous systems we generate the sinusoidal signal in (46) by the equation

$$\begin{bmatrix} \dot{x} \\ \dot{y} \end{bmatrix} = \begin{bmatrix} \mu & \omega \\ -\omega & \mu \end{bmatrix} \begin{bmatrix} x \\ y \end{bmatrix} - (x^2 + y^2) \begin{bmatrix} 1 & 0 \\ 0 & 1 \end{bmatrix} \begin{bmatrix} x \\ y \end{bmatrix}, \tag{48}$$

which is the normal form of a supercritical Hopf bifurcation.[40] For $\mu = 1$ this leads to the stable nonlinear oscillations

$$\begin{bmatrix} x(t) \\ y(t) \end{bmatrix} = \begin{bmatrix} \sin(\omega t) \\ \cos(\omega t) \end{bmatrix}. \tag{49}$$

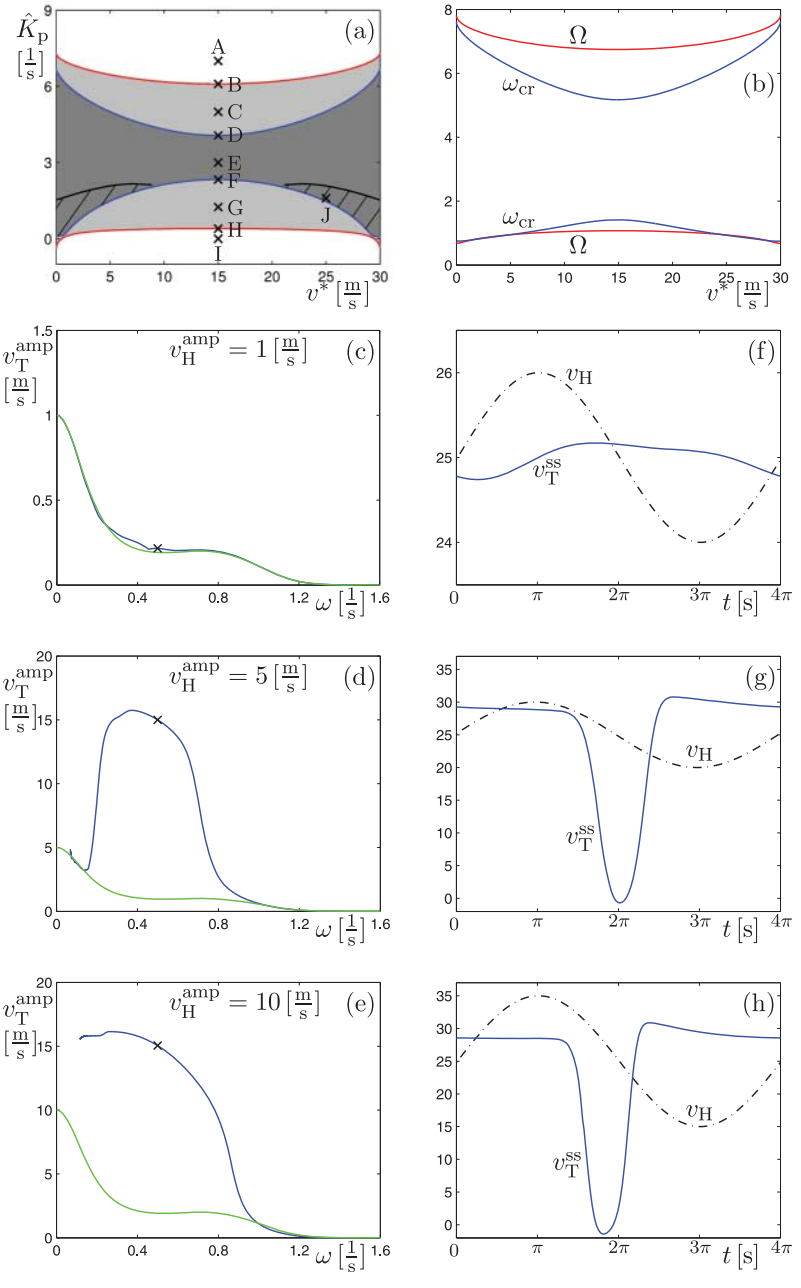

Figure 10. (a) Stability chart in the $(v^*, \hat{K}_p)$-plane for $\hat{K}_v = 0.5$ [1/s], $\hat{K}_i = 0.5$ [1/s^2] and $\sigma = 0.2$ [s] when using the range policy (2), (4) with parameters shown in Table A1. (b) Variation of the frequencies Ω and ω_{cr} along the linear plant and string stability boundaries. The same notation is used as in Figure 6(a), (b) and the bistable domain is indicated as dashed. (c)–(e) The amplitude of the steady-state oscillations of a vehicle at the tail of a $(85 + 1)$-car chain for different perturbation sizes applied at the head vehicle. The parameters correspond to the point marked J in panel (a). The blue curves are for the nonlinear model while the green curves show the linear approximation. (f)–(h) Velocity oscillations of the head vehicle (black dashed–dotted curve) and the tail vehicle in steady state (blue solid curve) corresponding to the crosses at $\omega = 0.5$ [1/s] in panels (c)–(e).

In Figure 10(c)–(e) the blue curve depicts the amplitude of the tail vehicle $v_{\mathrm{T}}^{\mathrm{amp}}$ as a function of the excitation frequency ω for different values of the amplitude of the head vehicle $v_{\mathrm{H}}^{\mathrm{amp}}$. The nonlinear results are compared with the prediction of the linear model (green curve) that is based on the transfer function (31). For small ω the blue curves are missing since a large number of collocation points were needed to represent the periodic orbit and the continuation tools lead to computational difficulties. The oscillations are plotted in Figure 10(f)–(h) for $\omega = 0.5$ [1/s]. When the excitation amplitude is small (Figure 10(c), (f)) the linear model gives a good prediction and string stable behaviour is observed at all frequencies, that is, perturbations are attenuated as they propagate along the chain of vehicles. On the other hand, when the excitation amplitude exceeds a critical value (Figure 10(d), (g)), then the system becomes string unstable. That is, perturbations may increase as they propagate upstream and lead to large-amplitude stop-and-go oscillations at the tail. Further increasing the oscillation amplitude (Figure 10(e), (h)), no significant changes are observed in the qualitative dynamics. These results correspond to what was observed in [26] for a simplified model using a ring configuration. We remark that the acceleration of vehicles may become unrealistically large and the speed may become slightly negative for the fully developed stop-and-go motion since the engine and break torques are not saturated in our model. Investigating such effects are left for future research.

The domains of bistability are indicated in Figure 10(a) as dashed regions bounded by the linear string stability boundaries (blue curves) and the bistability boundaries (black curves), the latter one obtained by numerical continuation. When moving from the linear stability boundary towards the bistability boundary, the size of the input perturbation required to trigger large-amplitude oscillations increases. In the vicinity of the linear stability curve even small perturbations at the head lead to stop-and-go oscillations at the tail. On the other hand, close to the bistability boundary the input at the head has to be almost as large the output at the tail. By observing the shape of the bistable regime one may notice that considering the linear string stability boundaries in the worst-case scenario ($v^* \approx 15$[m/s]) is adequate to make the system string stable for all v^* values at the nonlinear level. This property allows a reliable nonlinear CCC design.

5. Conclusion and discussion

In this paper, we established the concept of CCC that goes beyond traditional platooning scenarios and allows modular and scalable design of heterogenous CVS. In particular, we showed that using CCC, one can exploit the ad-hoc nature of wireless V2V communication and ensure the existence of a uniform flow equilibrium in the entire velocity range independent of the external disturbances, connectivity structure, applied control gains, and communication delays. We demonstrated that designing the nonlinear range policy appropriately may lead to increased flux on highways while the flow can be stabilised by tuning the gains in the proposed nonlinear, multi-input, PIVA controllers. We explained how time delays arise in the feedback loops corresponding to intermittencies and packet drops.

We analysed the linear and nonlinear dynamics of a CVS built as a concatenation of the simplest CCC configuration. In particular, we evaluated the plant and string stability of the system. At the linear level we used transfer functions to evaluate the dynamics

and converted the algebraic stability conditions into stability charts that allow designers to choose the control gains. We also proved that if the communication delay exceeds the half of the time headway then no combinations of the proportional, integral, and velocity gains can ensure string stability. We used numerical continuation to evaluate the dynamics at the nonlinear level and to characterise the domains of bistability in parameter space. In these domains the system showed string stable behaviour for small perturbations, that is, perturbations decayed as they propagated backward along the chain of vehicles. On the other hand, for large perturbations we observed string instability and stop-and-go motion arose as the signal cascaded backward. However, we also found that bistability can be avoided by selecting the control gains according to the worst-case scenario of linear stability, making the nonlinear control design successful.

Indeed, many interesting questions remain to be studied about CCC and CVS. For example, acceleration may be used to improve the performance, especially to increase the critical delay.[36] Also, it can be shown that string stability may be achieved by exploiting long range V2V communication even when the vehicles between the sender and the receiver are human-driven cars that are not equipped with range sensors and communication.[35] Finally, by analysing the covariance dynamics one may design controllers that ensure plant stability as well as attenuation of disturbances despite stochastic delay variations in the control loop.[34] Showing the applicability of these results on physics-based vehicle models and realising the controllers on real vehicles will be pursued in the future.

Acknowledgments

The author acknowledges the discussions with Sergei Avedisov, Jin Ge, Chaozhe He, Nan Li, Wubing Qin, Shrenik Shah, and Linjun Zhang.

Disclosure statement

No potential conflict of interest was reported by the authors.

Funding information

This research was supported by the National Science Foundation (award #1351456).

References

[1] Schrank D,Eisele B, Lomax T. 2012 Annual urban mobility report. Texas A&M Transportation Institute; 2012. Available from: http://mobility.tamu.edu/ums/.
[2] Caveney D. Cooperative vehicular safety applications. IEEE Control Syst Mag. 2010;30:38–53.
[3] University of Michigan Transportation Research Institute. Safety Pilot; 2012. Available from: http://safetypilot.umtri.umich.edu/.
[4] Chan E, Gilhead P, Jelinek P, Krejci P, Robinson T. Cooperative control of SARTRE automated platoon vehicles. Paper presented at: Proceedings of the 19th ITS World Congress, Vienna; 2012.
[5] van Nunen E, Kwakkernaat RJAE, Ploeg J, Netten BD. Cooperative competition for future mobility. IEEE Trans Intell Transp Syst. 2012;13:1018–1025.
[6] Geiger A, Lauer M, Moosmann F, et al. Team AnnieWAY's entry to the 2011 grand cooperative driving challenge. IEEE Trans Intell Transp Syst.. 2012;13:1008–1017.

[7] Alam A, Besselink B, Turri V, Mårtensson J, Johansson KH. Heavy-duty vehicle platooning towards sustainable freight transportation: a cooperative method to enhance safety and efficiency. IEEE Control Syst Mag. 2015;36:34–56.
[8] Lidström K, Sjöberg K, Holmberg U, et al. A modular CACC system integration and design. IEEE Trans Intell Transp Syst. 2012;13:1050–1061.
[9] Milanes V, Shladover SE, Spring J, Nowakowski C, Kawazoe H, Nakamura M. Cooperative adaptive cruise control in real traffic situations. IEEE Trans Intell Transp Syst. 2014;15:296–305.
[10] Naus GJL, Vugts RPA, Ploeg J, van de Molengraft MJG, Steinbuch M. String-stable CACC design and experimental validation: A frequency-domain approach. IEEE Trans Veh Technol. 2010;59:4268–4279.
[11] Wang M, Treiber M, Daamen W, Hoogendoorn SP, van Arem B. Modelling supported driving as an optimal control cycle: framework and model characteristics. Transp Res C. 2013;36:547–563.
[12] Wang M, Daamen W, Hoogendoorn SP, van Arem B. Rolling horizon control framework for driver assistance systems. Part I: mathematical formulation and non-cooperative systems. Transp Res C. 2014;40:271–289.
[13] Wang M, Daamen W, Hoogendoorn SP, van Arem B. Rolling horizon control framework for driver assistance systems. Part II: cooperative sensing and cooperative control. Transp Res C. 2014;40:290–311.
[14] Ploeg J, van de Wouw N, Nijmeijer H. $\mathcal{L}_p$ string stability of cascaded systems: application to vehicle platooning. IEEE Trans Control Syst Technol.. 2014;22:786–793.
[15] Ploeg J, Shukla DP, van de Wouw N, Nijmeijer H. Controller synthesis for string stability of vehicle platoons. IEEE Trans Intell Transp Syst. 2014;15:854–865.
[16] Öncü S, Ploeg J, van de Wouw N, Nijmeijer H. Cooperative adaptive cruise control: network-aware analysis of string stability. IEEE Trans Intell Transp Syst. 2014;15:1527–1537.
[17] di Bernardo M, Salvi A, Santini S. Distributed consensus strategy for platooning of vehicles in the presence of time varying heterogeneous communication delays. IEEE Trans Intell Transp Syst. 2015;16:102–112.
[18] Orosz G, Shah SP. A nonlinear modeling framework for autonomous cruise control. Paper presented at: Proceedings of the ASME Dynamical Systems and Control Conference. Paper no. DSCC2012-MOVIC2012-8871 ASME; 2012. pp. 467–471.
[19] Davis LC. Stability of adaptive cruise control systems taking account of vehicle response time and delay. Phys Lett A. 2012;376:2658–2662.
[20] Davis LC. Optimality and oscillations near the edge of stability in the dynamics of autonomous vehicle platoons. Phys A. 2013;392:3755–3764.
[21] Davis LC. The effects of mechanical response on the dynamics and string stability of a platoon of adaptive cruise control vehicles. Phys A. 2013;392:3798–3805.
[22] Ulsoy AG, Peng H, Çakmakci M. Automotive control systems. Cambridge: Cambridge University Press; 2012.
[23] Naus GJL, Vugts RPA, Ploeg J, van de Molengraft MJG, Steinbuch M. Hierarchical platoon control with heterogeneous information feedback. Control Theory Appl. 2011;5:1766–1781.
[24] Bai F, Krishnan H. Reliability analysis of DSRC wireless communication for vehicle safety applications. Paper presented at: Proceedings of the IEEE Intelligent Transportation Systems Conference, Toronto; 2006. pp. 355–362.
[25] Orosz G, Wilson RE, Stépán G. Traffic jams: dynamics and control. Philos Trans R Soc A. 2010;368:4455–4479.
[26] Orosz G, Wilson RE, Szalai R, Stépán G. Exciting traffic jams: nonlinear phenomena behind traffic jam formation on highways. Phys Rev E. 2009;80:046205.
[27] Orosz G, Moehlis J, Bullo F. Robotic reactions: delay-induced patterns in autonomous vehicle systems. Phys Rev E. 2010;81:025204(R).
[28] Szalai R, Orosz G. Decomposing the dynamics of heterogeneous delayed networks with applications to connected vehicle systems. Phys Rev E. 2013;88:040902(R).
[29] Wilson RE, Berg P, Hooper S, Lunt G. Many-neighbour interaction and non-locality in traffic models. Eur Phys J B. 2004;39:397–408.

[30] Wilson RE. Mechanisms for spatio-temporal pattern formation in highway traffic models. Philos Trans R Soc A. 2008;366:2017–2032.
[31] He CR, Maurer H, Orosz G. Fuel consumption optimization of heavy-duty vehicles with grade, wind, and traffic information. ASME J Comput Nonlinear Dyn. 2016; p. accepted.
[32] Huang CL, Fallah YP, Sengupta R, Krishnan H. Adaptive intervehicle communication control for cooperative safety systems. IEEE Netw. 2010;24:6–13.
[33] Insperger T, Stépán G, Semi-discretization for time-delay systems: stability and engineering applications, Appl Math Sci, Vol. 178 Springer, 2011.
[34] Qin WB, Gomez MM, Orosz G. Stability and frequency response under stochastic communication delays with applications to connected cruise control design. IEEE Transactions of Intelligent Transportation Systems. 2016;p. accepted.
[35] Zhang L, Orosz G. Motif-based analysis of connected vehicle systems: delay effects and stability. IEEE Trans Intell Transp Syst. 2016;17:1638–1651.
[36] Ge JI, Orosz G. Dynamics of connected vehicle systems with delayed acceleration feedback. Transp Res C. 2014;46:46–64.
[37] Stépán G, Retarded dynamical systems: stability and characteristic functions. Pitman Research Notes in Mathematics, Vol. 210 Longman, 1989.
[38] Engelborghs K, Luzyanina T, Samaey G. DDE-BIFTOOL v. 2.00: a Matlab package for bifurcation analysis of delay differential equations. TW-330, Department of Computer Science, Katholieke Universiteit Leuven, Belgium; 2001. Available from: http://twr.cs.kuleuven.be/research/software/delay/ddebiftool.shtml.
[39] Roose D, Szalai R. Continuation and bifurcation analysis of delay differential equations. Krauskopf B, Osinga HM, Galan-Vioque J, editors. Understanding complex systems. New York: Springer, 2007, p. 359–399.
[40] Guckenheimer J, Holmes P, Nonlinear oscillations, dynamical systems, and bifurcations of vector fields. Appl Math Sci. Vol. 42 Springer, 1983.
[41] Attard WP, Bassett M, Parsons P, Blaxill H. A new combustion system achieving high drive cycle fuel economy improvements in a modern vehicle powertrain. Paper presented at: Proceedings of the SAE 2011 World Congress & Exhibition, 2011-01-0664; 2011.
[42] Qin WB, Orosz G. Digital effects and delays in connected vehicles: linear stability and simulations. In: Paper presented at: Proceedings of the ASME Dynamical Systems and Control Conference. Paper no. DSCC2013-3830 ASME; 2013. p. V003T30A001.

Appendix 1. Parameters used in this paper

Table A1. Data of a 2011 Chevrolet HHR vehicle [41] are shown together with the parameters used for the range policies (2)–(5).

$m = 1555$ (kg)	Mass of the vehicle
$C_d = 0.34$	Air drag coefficient
$A = 2.3$ (m^2)	Frontal area
$\rho_a = 1.184$(kg/m^3)	Air density at 25 (°C)
$k = \frac{1}{2} C_d \rho_a A = 0.463$ (kg/m)	
$R = 0.313$ (m)	Tire rolling radius
$\gamma = 0.011$	Tire rolling resistance coefficient
$g = 9.81$ (m/s^2)	Gravitational constant
$\ell = 5$(m)	Vehicle length (approximation)
$v_{max} = 30$(m/s)	Desired maximum velocity
$h_{st} = 5$(m)	Desired stopping distance
$h_{go} = 35$(m)	Minimal free-flow distance

Appendix 2. Digital control with zero-order hold and no packet drops

As mentioned in the main text, σ-s in (6), (14) represent the average delays while the delay in fact varies in time; see Figure 3. In order to demonstrate that this is a reasonable approximation we present the linear stability charts for the predecessor–follower configuration analysed in Section 3 with no packet drops; see Figure 3(a) and (12) with $r = 1$.

In this case the system (17) is substituted by

$$\begin{aligned}
\dot{h}(t) &= v_{\mathrm{L}}(t) - v(t),\\
\dot{v}(t) &= -\gamma\, g - \frac{k}{m} v^2(t) + \hat{K}_{\mathrm{p}}(V(h(t_{k-1})) - v(t_{k-1})) + \hat{K}_{\mathrm{i}} z(t_k)\\
&\quad + \hat{K}_{\mathrm{v}}(W(v_{\mathrm{L}}(t_{k-1})) - v(t_{k-1})) + \hat{K}_{\mathrm{a}} \dot{v}_{\mathrm{L}}(t_{k-1}),\\
z(t_{k+1}) &= z(t_k) + (V(h(t_k)) - v(t_k))\Delta t,
\end{aligned} \tag{A1}$$

on the time interval $t \in [k\,\Delta t, (k+1)\Delta t)$ where the integral part of controller is implemented as a discrete map. Again we consider $\hat{K}_{\mathrm{a}} = 0$ and linearise the system about the equilibrium (20). Then we solve the linearised system on the time interval $t \in [k\,\Delta t, (k+1)\Delta t)$ with the approximation $\int_{t_k}^{t_{k+1}} \tilde{v}_{\mathrm{L}}(t)\mathrm{d}t \approx (\tilde{v}_{\mathrm{L}}(t_{k+1}) + \tilde{v}_{\mathrm{L}}(t_k))\Delta t/2$ and define the augmented state and input

$$\hat{x}(k) = \begin{bmatrix} \tilde{h}(t_k)\\ \tilde{v}(t_k)\\ \tilde{z}(t_k)\\ \tilde{h}(t_{k-1})\\ \tilde{v}(t_{k-1}) \end{bmatrix} = \begin{bmatrix} h(t_k) - h^*\\ v(t_k) - v^*\\ z(t_k) - z^*\\ h(t_{k-1}) - h^*\\ v(t_{k-1}) - v^* \end{bmatrix}, \quad \hat{u}(k) = \tilde{v}_{\mathrm{L}}(t_k) = v_{\mathrm{L}}(t_k) - v^*, \tag{A2}$$

to obtain the form

$$\hat{x}(k+1) = \hat{\mathbf{A}}\,\hat{x}(k) + \hat{\mathbf{B}}_{-1}\,\hat{u}(k-1) + \hat{\mathbf{B}}_0\,\hat{u}(k) + \hat{\mathbf{B}}_1\,\hat{u}(k+1). \tag{A3}$$

Here the matrices

$$\begin{aligned}
\hat{\mathbf{A}} &= \begin{bmatrix} 1 & -\alpha_1 & \alpha_2\hat{K}_{\mathrm{i}} & \alpha_2\hat{K}_{\mathrm{p}}N_* & -\alpha_2(\hat{K}_{\mathrm{p}} + \hat{K}_{\mathrm{v}})\\ 0 & \alpha_0 & \alpha_1\hat{K}_{\mathrm{i}} & \alpha_1\hat{K}_{\mathrm{p}}N_* & -\alpha_1(\hat{K}_{\mathrm{p}} + \hat{K}_{\mathrm{v}})\\ N_*\Delta t & -\Delta t & 1 & 0 & 0\\ 1 & 0 & 0 & 0 & 0\\ 0 & 1 & 0 & 0 & 0 \end{bmatrix},\\
\hat{\mathbf{B}}_{-1} &= \begin{bmatrix} \alpha_2\hat{K}_{\mathrm{v}}\\ \alpha_1\hat{K}_{\mathrm{v}}\\ 0\\ 0\\ 0 \end{bmatrix}, \quad \hat{\mathbf{B}}_0 = \hat{\mathbf{B}}_1 = \begin{bmatrix} \Delta t/2\\ 0\\ 0\\ 0\\ 0 \end{bmatrix},
\end{aligned} \tag{A4}$$

contain the coefficients

$$\alpha_0 = \exp\left(-2\frac{k}{m}v^*\Delta t\right), \quad \alpha_1 = \frac{1-\alpha_0}{2(k/m)v^*}, \quad \alpha_2 = \frac{\alpha_1 - \Delta t}{2(k/m)v^*}. \tag{A5}$$

The output $\hat{y}(k) = \tilde{v}(t_k) = v(t_k) - v^*$ can be formally written as

$$\hat{y}(k) = \hat{\mathbf{C}}\hat{y}(k), \quad \hat{\mathbf{C}} = [0\ \ 1\ \ 0\ \ 0\ \ 0]. \tag{A6}$$

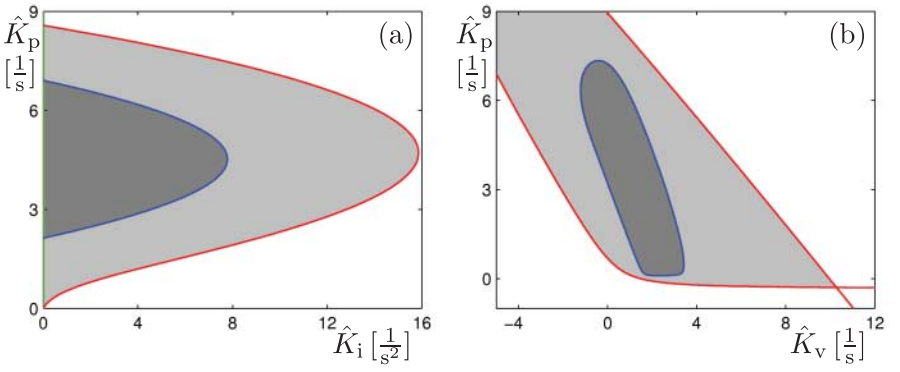

Figure A1. Stability diagrams using ZOH with sampling time $\Delta t = 0.1$ [s]. (a) Stability chart in the $(\hat{K}_i, \hat{K}_p)$-plane for $\hat{K}_v = 0.5$ [1/s]; cf. Figure 7(b). (b) Stability chart in the $(\hat{K}_v, \hat{K}_p)$-plane for $\hat{K}_i = 0.5$ [1/s^2]; cf. Figure 8(b). The same notation is used as in Figure 6(a), (b).

Taking the Z-transform of (A3) and (A6) with zero initial conditions and using the matrices (A4) yields the transfer function

$$\begin{aligned}\hat{\Gamma}(z) = \frac{\tilde{V}(z)}{\tilde{V}_L(z)} &= \hat{\mathbf{C}}(z\mathbf{I} - \hat{\mathbf{A}})^{-1}(\hat{\mathbf{B}}_{-1}/z + \hat{\mathbf{B}}_0 + \hat{\mathbf{B}}_1 z) \\ &= \frac{c_2 z^2 + c_1 z + c_0}{z^4 + a_3 z^3 + a_2 z^2 + a_1 z + a_0}.\end{aligned} \tag{A7}$$

where

$$\begin{aligned}
a_3 &= -\alpha_0 - 2, \\
a_2 &= \hat{K}_p(\alpha_1 - \alpha_2 N_*) + \hat{K}_i(\alpha_1 - \alpha_2 N_*)\Delta t + \hat{K}_v\alpha_1 + 2\alpha_0 + 1, \\
a_1 &= -\hat{K}_p(2\alpha_1 - (\alpha_1^2 + \alpha_0\alpha_2 + \alpha_2)N_*) - \hat{K}_i(\alpha_1 - (\alpha_1^2 + \alpha_0\alpha_2)N_*)\Delta t - \hat{K}_v 2\alpha_1 - \alpha_0, \\
a_0 &= \hat{K}_p(\alpha_1 - (\alpha_1^2 + \alpha_0\alpha_2)N_*) + \hat{K}_v\alpha_1, \\
c_2 &= \hat{K}_p\alpha_1 N_*\Delta t/2 + \hat{K}_i\alpha_1 N_*\Delta t^2/2 + \hat{K}_v\alpha_1, \\
c_1 &= \hat{K}_i\alpha_1 N_*\Delta t^2/2 - \hat{K}_v 2\alpha_1, \\
c_0 &= -\hat{K}_p\alpha_1 N_*\Delta t/2 + \hat{K}_v\alpha_1.
\end{aligned} \tag{A8}$$

The transfer function (47) can be used to analyse plant stability and string stability.[42] In particular, plant stability requires that all poles (roots of the denominator) are located within the unit circle while string stability requires $|\hat{\Gamma}(e^{i\omega\Delta t})| < 1$ for all $\omega > 0$; cf. (36). These conditions can be checked by using the methods presented in the paper and the corresponding stability diagrams are shown in Figure A1 for the sampling time $\Delta t = 0.1$ [s]. When comparing these with Figures 7(b) and 8(b) made for the average delay $\sigma = 3\Delta t/2 = 0.15$ [s] the similarity is remarkable, while the complexity of the formulae (A7), (A8), (A5) is much higher than that of (31).

Appendix 3. First-order lag approximation

Considering the approximation (19) and defining the variable $w = T_{\text{en}}\eta/mR$, (1), (14)–(16) result in the ordinary differential equations

$$\begin{aligned}
\dot{h}(t) &= v_{\text{L}}(t) - v(t),\\
\dot{v}(t) &= -\gamma\, g - \frac{k}{m}v^2(t) + w(t),\\
\dot{z}(t) &= V(h(t)) - v(t),\\
\dot{w}(t) &= \frac{1}{\sigma}(\hat{K}_{\text{p}}\dot{z}(t) + \hat{K}_{\text{i}}z(t) + \hat{K}_{\text{v}}(W(v_{\text{L}}(t) - v(t)) + \hat{K}_{\text{a}}\dot{v}_{\text{L}}(t) - w(t)),
\end{aligned} \tag{A9}$$

where $\hat{K}_{\text{p}}$, $\hat{K}_{\text{i}}$, $\hat{K}_{\text{v}}$, $\hat{K}_{\text{a}}$ are defined by (18) and we still consider the simplifications $\phi = 0$, $v_{\text{w}} = 0$ and $J = 0 \Longrightarrow m_{\text{eff}} = m$ (cf. (17)). Also, let us assume $\hat{K}_{\text{a}} = 0$. The equilibrium of (A9) is given by (20) and $w^* = \hat{K}_{\text{i}}z^*$. Extending the state vector in (21) by incorporating $\tilde{w}(t) = w(t) - w^*$ as the fourth component, that is, defining $\bar{x}(t) = [\,\tilde{h}(t),\ \tilde{v}(t),\ \tilde{z}(t),\ \tilde{w}(t)]^{\text{T}}$, while still using the input $u(t) = \tilde{v}_{\text{L}}(t)$ and the output $y(t) = \tilde{v}(t)$, one may linearise (A9) and obtain

$$\begin{aligned}
\dot{\bar{x}}(t) &= \bar{\mathbf{A}}\,\bar{x}(t) + \bar{\mathbf{B}}\,u(t),\\
y(t) &= \bar{\mathbf{C}}\,\bar{x}(t) + \bar{\mathbf{D}}\,u(t),
\end{aligned} \tag{A10}$$

with matrices

$$\begin{aligned}
\bar{\mathbf{A}} &= \begin{bmatrix} 0 & -1 & 0 & 0\\ 0 & -2\dfrac{k}{m}v^* & 0 & 1\\ N_* & -1 & 0 & 0\\ N_*\dfrac{1}{\sigma}\hat{K}_{\text{p}} & -\dfrac{1}{\sigma}(\hat{K}_{\text{p}} + \hat{K}_{\text{v}}) & \dfrac{1}{\sigma}\hat{K}_{\text{i}} & -\dfrac{1}{\sigma} \end{bmatrix},\\
\bar{\mathbf{B}} &= \begin{bmatrix} 1\\ 0\\ 0\\ \dfrac{1}{\sigma}\hat{K}_{\text{v}} \end{bmatrix}, \quad \bar{\mathbf{C}} = \begin{bmatrix} 0 & 1 & 0 & 0 \end{bmatrix}, \quad \bar{\mathbf{D}} = 0.
\end{aligned} \tag{A11}$$

The Laplace transform of (A10) with zero initial conditions yields the transfer function

$$\begin{aligned}
\Gamma(s) &= \frac{\tilde{V}(s)}{\tilde{V}_{\text{L}}(s)} = \bar{\mathbf{C}}(s\mathbf{I} - \bar{\mathbf{A}})^{-1}\bar{\mathbf{B}} + \bar{\mathbf{D}}\\
&= \frac{\hat{K}_{\text{v}}s^2 + N_*\hat{K}_{\text{p}}s + N_*\hat{K}_{\text{i}}}{\sigma\, s^4 + (\sigma\, 2(k/m)v^* + 1)s^3 + (2(k/m)v^* + \hat{K}_{\text{p}} + \hat{K}_{\text{v}})s^2 + (N_*\hat{K}_{\text{p}} + \hat{K}_{\text{i}})s + N_*\hat{K}_{\text{i}}}.
\end{aligned} \tag{A12}$$